Chemical Engineering Journal 535 (2026) 174990

Contents lists available at ScienceDirect

Chemical Engineering Journal

journal homepage: www.elsevier.com/locate/cej

Isolation-to-delivery hydrogel enables efficient isolation and sustained release of exosomes to enhance wound healing

Lihua Yang [a], Cenlong Huang [a], Mingwei Shen [a], Chenyu Xu [a], Zonglin Guo [b], Juan Gallo [c], Meijin Guo [a,*], Ali Mohsin [a,**]

[a] State Key Laboratory of Bioreactor Engineering, East China University of Science and Technology, Shanghai, 200237, China
[b] College of Food Science, South China Agricultural University, Guangzhou, 510642, China
[c] International Iberian Nanotechnology Laboratory, Av. Mestre José Veiga s/n, 4715-330, Braga, Portugal

ARTICLE INFO

Keywords:
Hydrogel
Pullulan
Sodium alginate
Exosome isolation
Controlled release

ABSTRACT

Promoting rapid wound healing is essential for preventing hypertrophic scars. Exosome-based therapies represent a promising approach for improving healing outcomes, but they encounter significant challenges: 1) the isolation of exosomes requires complex, time-consuming, and costly procedures; 2) the stability of exosomes is limited due to the pH- and temperature-sensitive nature of their lipid bilayer. Hydrogels, known for their hydrophilic and porous architectures, offer an attractive solution by enabling the isolation of exosomes from macromolecular impurities while simultaneously protecting them from degradation. In this study, we designed a bilayer polysaccharide hydrogel where pullulan (PL) and calcium ions (Ca) form the inner core, while sodium alginate (SA) creates an effective isolating gel in the exosome-containing precursor solution. By integrating freeze-drying with ultrasonic-assisted dissolution, the approach effectively achieves both the isolation and controlled release of exosomes. The results show that the PL + Ca + SA hydrogel exhibits superior gelation stability compared to other formulations. During isolation, the PL + Ca + SA hydrogel efficiently enriched exosomes while maintaining their characteristic "teacup-shaped" morphology and protein markers. The isolation yield (87.2%) was comparable to that obtained by ultracentrifugation, with no significant differences in particle number or impurities. Furthermore, ultrasonic-assisted dissolution enabled sustained exosome release for at least 7 days, as predicted by the Higuchi diffusion model. Functionally, the EXO@PL + Ca + SA hydrogel enhanced fibroblast proliferation and viability for up to one week, changing the ROS content (decreasing 92%) and the COL-I/COL-III ratio to 0.58 of mouse wound model. Furthermore, transcriptomic analysis revealed significant alterations in related pathways involving key genes. Overall, this bilayer hydrogel offers an integrated platform for exosome isolation and controlled delivery, providing preliminary experimental evidence to support further translational research.

1. Introduction

The rapid healing of wounds represents a critical clinical concern that necessitates immediate attention [1]. Insufficient healing can result in various dermatological complications, such as hypertrophic scars, which significantly affect both the physical and psychological health of patients [2]. Application of exosomes has emerged as a well-established treatment modality for wound healing and has been extensively utilized for both acute and chronic wound care [3]. Exosomes are extracellular vesicles with diameters ranging from 40 to 160 nm, comprising an array of bioactive constituents including nucleic acids, proteins, lipids, and miRNA [4]. These extracellular vesicles play a significant role in intercellular communication, immune regulation, tissue repair and regeneration, and have been proposed as tools for disease diagnosis and detection, among other applications [5]. Furthermore, these exosomes are particularly beneficial for promoting vascular regeneration and collagen formation during the wound healing process [6]. Exosomes can originate from diverse sources, including various tissues and organs, as well as animal and plant cells [7]. However, their practical application is often limited by challenges related to isolation and delivery

* Correspondence to: M. Guo, P.O. Box 329#, East China University of Science and Technology, 130 Meilong Rd., Shanghai, 200237, China.
** Correspondence to: A. Mohsin, East China University of Science and Technology, 130 Meilong Rd., Shanghai, 200237, China.
E-mail addresses: guo_mj@ecust.edu.cn (M. Guo), alimohsin@ecust.edu.cn (A. Mohsin).

https://doi.org/10.1016/j.cej.2026.174990
Received 6 January 2026; Received in revised form 24 February 2026; Accepted 6 March 2026
Available online 8 March 2026
1385-8947/© 2026 Elsevier B.V. All rights are reserved, including those for text and data mining, AI training, and similar technologies.

methodologies.

Although ultracentrifugation is regarded as the gold standard method for exosome isolation, it is impractical for industrial-scale use due to its long processing times, expensive equipment, and low extraction yields [8]. Meanwhile, alternative techniques such as PEG precipitation, ultrafiltration, volumetric exclusion chromatography, or immunoaffinity capture are also unsuitable for large-scale manufacturing due to their low isolation rate [9]. Thus, current exosome isolation techniques possess inherent limitations and do not adhere to standardized criteria for the storage and preservation of exosomes. Isolated exosomes are typically frozen at −80 °C for long-term storage; however, extreme temperatures have the potential to destabilize the lipid bilayer membrane, resulting in the premature degradation of encapsulated bioactive compounds and thereby compromising their biological activity during subsequent delivery [10]. Therefore, exploring effective methods for isolating exosomes and enhancing their stability during storage and delivery is a critical area of scientific research.

Hydrogels are three-dimensional network materials formed by cross-linking hydrophilic high-molecular weight polymer chains [11,12]. The primary raw materials utilized in the production of hydrogels are proteins and polysaccharides that are derived from natural sources. Among these, natural polysaccharides are preferred due to their excellent plasticity and biological safety, especially when compared to proteins, which tend to present a higher degradation rate under varying temperature and pH conditions [13]. Polysaccharides can form physical cross-links through intermolecular forces or can be covalently coupled to form hydrogels through chemical cross-linking agents [14]. Although chemical crosslinking exhibits better stability than physical crosslinking [15], its bonding and dynamic equilibrium reconstruction speeds are slow, rendering it unsuitable for capturing active molecules. Therefore, physically cross-linked hydrogels made of natural polysaccharides and metal ions have become a prominent area of research. For example, the preparation of hydrogels from sodium alginate (SA)/carboxymethyl chitosan/gelatin and loading naringenin using calcium ions (Ca) as crosslinking agents has achieved remarkable results in the treatment of gastric diseases [16]. In addition, Chen et al. (2024) prepared composite hydrogel microspheres using SA and Ca for the removal of heavy metal ions from wastewater [17]. Although SA: Ca hydrogels exhibit a high capacity for the isolation of compounds, they present a high retention rate for water molecules due to their ‘egg-box’ like hollow structure, which is unsuitable for exosome capture. Pullulan (PL) is a neutral, biodegradable, non-toxic, non-immunogenic, and non-ionic polysaccharide with a unique connection mode to its main chain structure, which results in excellent mechanical properties and a very high biofilm adhesion force [18]. Previous research works have revealed that, although the ether C—O group present in PL can form ionic bonds with metal ions, methyl groups and other molecular structures, its overall structure is relatively unstable and susceptible to degradation due to environmental factors [19]. Due to this environmental responsiveness, PL often requires formulation with other compounds to enhance hydrogel stability [20]. Therefore, there is a dire need to investigate the development of a bilayer grid-like hydrogel with PL + Ca as the core components, in combination with SA, to facilitate the simultaneous isolation and delivery of exosomes.

Moreover, previous studies have shown that ice crystal sublimation during freeze-drying in hydrogels can cause gel collapse and shrinkage, reducing the uniformity of crosslinking [21]. Although rehydration reverts the hydrogel to its double-layer grid structure, this phenomenon can adversely affect the delivery and application of trapped exosomes. Ultrasonic-assisted dissolution is proposed as a viable solution to mitigate this phenomena. Ultrasonic stimulation at a certain frequency and intensity can produce cavitation effects, cause local high temperature and high pressure, and simultaneously generate strong shear forces [22]. These mechanical forces are expected to break the coordination bonds between SA and Ca, reducing the gel-forming capacity of PL + Ca + SA. The formation of a stable hydrogel, predominantly consisting of PL + Ca, is expected to enhance both the delivery efficiency of exosomes and the absorbability of the hydrogel.

In this study, we introduce a multifunctional hydrogel that simultaneously isolates, stabilizes, and controllably releases exosomes (Fig. 1), significantly enhancing wound healing and offering a transformative strategy for exosome-based biomaterial production. Using acute wounds in mice as a model, the therapeutic effect of EXO@PL + Ca + SA hydrogel on healing is discussed. This multifunctional pullulan/sodium alginate hydrogel system was utilized for the isolation, stabilization, and controlled release of exosomes for the first time. In short, this study offers an innovative strategy for industrial production and application of exosomes by designing a novel exosome hydrogel structure.

2. Materials and methods

2.1. Materials

Pullulan (CAS. 9057-02-7, viscosity: 124 Pa.s, molecular weight: 1.6 × 10^5 Da), sodium alginate (CAS.9005-38-3, viscosity: 969 Pa.s, M/G ratio of 1.6/2.0, molecular weight: 3.0 × 10^5 Da), and sodium chloride were procured from Henan Gaobao Industrial Co., Ltd., China. High-glucose medium (DMEM) and α-MEM basal medium were acquired from Suzhou Youyi Biotechnology Co., Ltd., China. Serum was obtained from Suzhou Ecosai Biotechnology Co., Ltd., China. Serum-free culture media were sourced from AventaCell BioMedical, USA. Antibiotic solutions were obtained from Gibco, USA. The ROS fluorescent probe (D2DCFDA) was purchased from MedChemExpress Biotechnology, USA. The AO Fluorescent Stain Kit was purchased from Solarbio, China.

2.2. Preparation of PL + Ca + SA composite hydrogel

The emulsion of pullulan polysaccharide (PL, 3 g) was prepared by dissolving the powder in 100 mL of deionized water under stirring (200 rpm/min) at room temperature (RT) for 30 min. Then, the calcium chloride powder (1 g) was stir-mixed with PL emulsion (100 rpm/min, RT for 30 min) to prepare PL + Ca hydrogel. Finally, the PL + Ca + SA hydrogel was prepared by mixing sodium alginate liquid (1 wt%) in the PL + Ca hydrogel at a ratio of 1:1, under stirring (100 rpm/min) at RT for 10 min [23]. After that, the PL + Ca + SA hydrogel was freeze-dried for 24 h (instrument: YTLG-12A-80, Shanghai Tuoye Technology Co., Ltd., China).

2.3. Preparation of EXO@PL + Ca + SA hydrogel

The EXO@PL + Ca + SA hydrogel was prepared as shown in Fig. S1. The supernatant containing exosomes was collected from UC-MSCs cell cultures, centrifuged (2000 ×*g*) at 4 °C for 10 min (Fig. 1A). Then, the supernatant was centrifuged again (10,000 ×*g*) at 4 °C for 30 min. This pretreated supernatant served as the solvent for hydrogel formation, as shown in Fig. 1B. For the detailed procedure, 3 g pullulan (PL) was dissolved in 100 mL of the pretreated supernatant and stirred at 200 rpm at room temperature (RT) for 30 min to form EXO@PL. Then, 1 g calcium chloride was mixed with EXO@PL at 100 rpm, RT, for 30 min to prepare EXO@PL + Ca hydrogel. Separately, 1 g sodium alginate (SA) was dissolved in 100 mL of pretreated cell culture. Finally, SA solution (1 wt%) was mixed with the PL + Ca hydrogel at a 1:1 ratio and stirred at 100 rpm, RT, for 10 min. The resulting EXO@PL + Ca + SA hydrogel was freeze-dried for 24 h using a YTLG-12A-80 instrument (Shanghai Tuoye Technology Co., Ltd., China).

2.4. Cell culture

Following euthanasia, mice were immersed in 75% alcohol for 5 min. The epidermal layer was carefully detached using surgical scissors and then rinsed in phosphate-buffered saline (PBS). The obtained epidermis

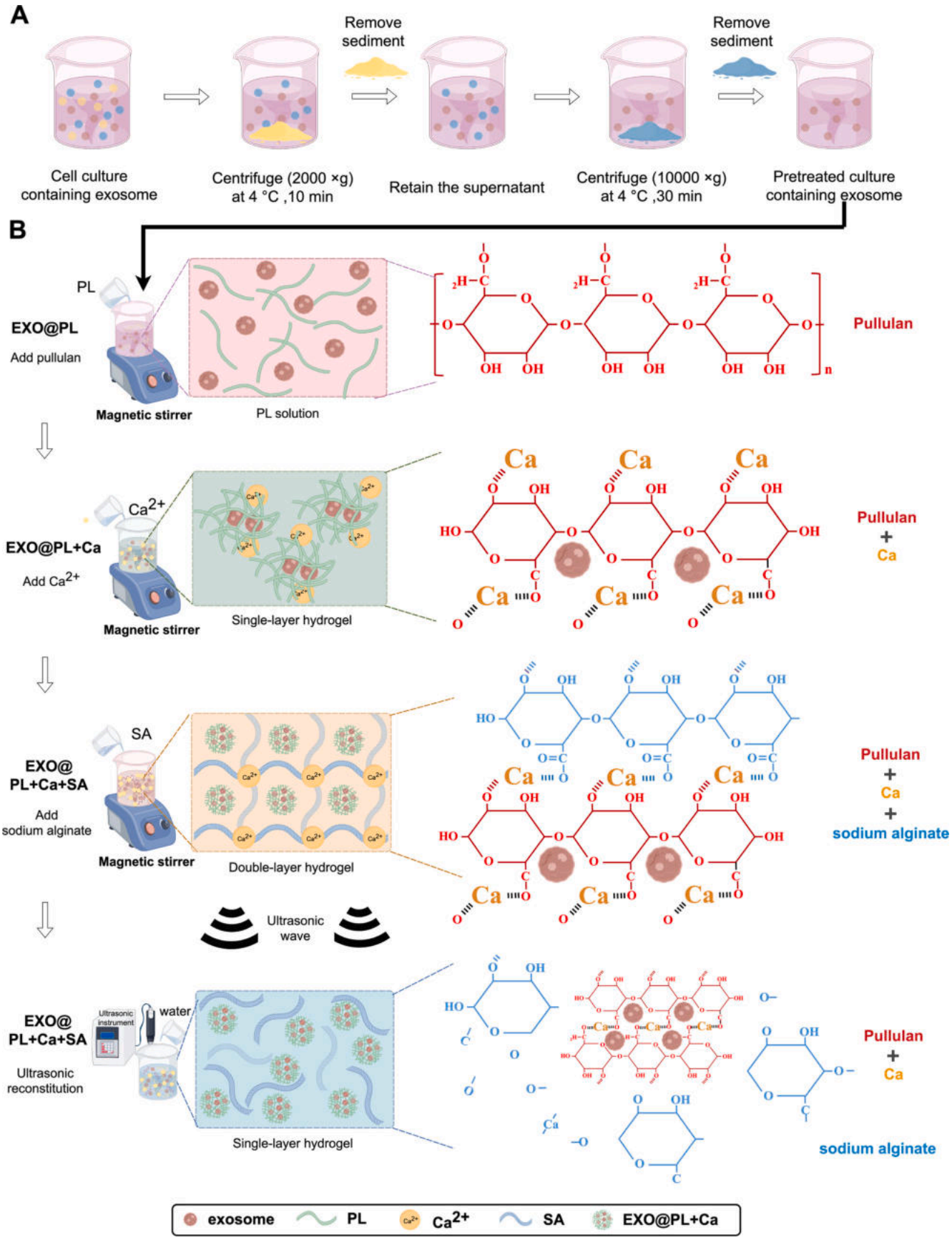

Fig. 1. Schematic diagram illustrating fabrication process and molecular structure of our prepared hydrogel combined with exosomes (EXO). A. Pretreatment of the liquid containing exosomes. B. Schematic diagram of the preparation process and delivery mechanism of hydrogel containing exosomes.

was cut into small pieces of approximately 1.0 mm × 1.0 mm, and the dermal fragments were subsequently placed into a 6.0 cm^2 cell culture dish. On the first day, 2 mL of complete culture medium consisting of DMEM (Suzhou Youyi Biotech, China) supplemented with 50% foetal bovine serum (Suzhou Ecosai Biotech, China) and 1.0% penicillin–streptomycin (Beyotime, China) was added, and the cells were incubated at 37 °C in a 5% CO_2 atmosphere. On the second day, an additional 6 mL of complete medium (DMEM containing 10% foetal bovine serum and 1.0% penicillin–streptomycin) was added. When the cell density reached approximately 50% confluence, fibroblasts (Fbs) began to migrate out from the tissue explants. The cells were then digested with 0.125% trypsin (Gibco, USA) to obtain passage 0 (P0) fibroblasts for subsequent experiments. Subsequently, the Passage 3 cells (16–20 × 10^4 cells/mL, CountStar, Alit Biotech, China) were cultured in 6-well plates for 48 h (Fig. S3), and the culture medium was treated with an exosome hydrogel at a ratio of 1:50 (v/v) to culture for an additional 48 h following medium renewal. The morphological development of the fibroblasts at various time points was examined utilizing an optical microscope (MF-52-N, Guangzhou Mingmei Optical Technology Co., Ltd., Guangdong, China).

2.5. Animal model

All C57BL/6 mice were acclimated under controlled laboratory conditions (22 ± 2 °C, 50 ± 5%, 12-h light/dark cycle) for a period of 7 days. Subsequently, the mice were randomly assigned to four groups, each comprising six subjects ($n = 6$). A 2.5 × 2.5 cm^2 area of hair was shaved from the skin using a razor, followed by the creation of circular wounds employing a 15 mm corneal drill and surgical scissors. The wounds were treated with PL + Ca + SA, EXO, and EXO@PL + Ca + SA on days 0, 2, 4, and 6. Wound healing progress was documented on days 0, 3, 7, 10, and 14. All surgical interventions conducted on the animals received approval from the Ethical Review Committee (No. 20241015 (12)) of Shanghai Ruitimos Biotechnology Co., Ltd. The maximum permissible wound size was set at 1000 mm^3, and wound size or trauma burden did not exceed this limit throughout the study.

2.6. Characterization of hydrogel

2.6.1. Freeze-dried moisture

The amount of water extracted by hydrogels indicates the efficacy of exosome isolation [24]. The hydrogel was weighed before drying, and the freeze-dried gel powder was weighed separately. The hydrogel concentration rate was then determined using the following formula. The isolation rate (ER%) was calculated as follows:

$$\mathrm{ER}\ (\%) = \left(1 - \frac{W_t}{W_0}\right) \times 100\%.$$

where W_t: weight of hydrogel powder after freeze-drying; W_0: weight of hydrogel before freeze-drying.

2.6.2. Ultraviolet spectroscopy

A volume of 500 μL of hydrogel samples (PL, PL + Ca, PL + SA, SA, SA + Ca, and PL + Ca + SA) was placed in a 1 mL cuvette. The wavelength spectrum parameters were set to detect the ultraviolet absorption peak using a UC-1600PC spectrophotometer (Jinan Jiangxue Medical Devices Co., Ltd., Shandong, China) of the hydrogel [25]. The preparation methods for the EXO, EXO@PL + Ca + SA hydrogel samples remained consistent with previous protocols. For the EXO + PL + Ca + SA liquid samples, the EXO liquid was added to the PL + Ca + SA hydrogels to ensure that the exosomes are located on the surface of the hydrogel rather than being embedded within.

2.6.3. FT-IR analysis

Hydrogel samples of PL, PL + Ca, PL + SA, SA, SA + Ca and PL + Ca + SA were mixed with KBr, ground to prepare the samples, and scanned using an infrared spectrometer (Nicolet iS5, ThermoFisher, America) [26]. The scanning range was 4000–400 cm^{-1}, and the resolution was 4 cm^{-1}.

2.6.4. Microstructure

A small quantity of hydrogel was taken and deposited onto a glass slide, and then the microscopic morphology and structure of the hydrogel were examined using an optical microscope (MF-52-N, Guangzhou Mingmei Optical Technology Co., Ltd., Guangdong, China) [26]. Imaging was performed in automatic exposure mode with monochrome settings development.

2.6.5. Rheological analysis

Hydrogels were prepared with 3 wt% pullulan, 1 wt% sodium alginate, and 1 wt% calcium chloride to investigate the effects of pullulan and sodium alginate on the gel-forming capabilities [27]. The mixture was stirred at a rate of 500 rpm /min and subsequently heated to 80 °C for 4 min. Immediately thereafter, the gel was poured into the cup rheometer. The rheometer is equipped with a circulating water system responsible for maintaining temperature control. The gel was allowed to stand for 15 min to restore its structure and achieve thermal equilibrium. All the samples were dissolved with deionized water, and the shear rate was varied from 0.1 to 100 s^{-1} at 25 °C. The storage modulus (G'), loss modulus (G"), and viscosity of the hydrogel solutions were measured via oscillation analysis.

2.6.6. Ultrasonic dissolution

An ultrasonic-assisted dissolution technique was employed to enhance the cleavage of sodium alginate and calcium ion bonds [28]. Following the freeze-drying of the PL + Ca + SA hydrogel using methodology 2.2, the resultant powder (0.1 g, 1 wt%) was dissolved in 10 mL of sterile deionized water. Ultrasonic treatment was conducted using an ultrasonic cleaning instrument (40 kHz, Sonics, Chicago, USA) at a power of 0, 200, 400, 600 W/L for a duration of 10 min. Consequently, the PL + Ca + SA dissolution solution was obtained.

2.6.7. Zeta potential

The zeta potential analysis of various samples, including freeze-dried powder (EXO@PL + Ca + SA, PL + Ca, 0.1 g), was performed by dissolving each sample into 10 mL deionized water [29]. The EXO@PL + Ca + SA hydrogels were treated with different ultrasonic wave powers (0, 200, 400, 600 W/L) for 10 min. The prepared samples were analyzed using a Zetasizer Nano ZS90 (Malvern Instruments, U.K.) maintained at 25 ± 0.1 °C. After preparation, the dispersions were carefully transferred into disposable U-shaped polystyrene cells supplied by Malvern for analysis. Each reported zeta potential value represents the average of three independent measurements to ensure accuracy and reproducibility.

2.6.8. Characterization of exosomes

EXO@PL + Ca + SA samples were ultrasonicated at 600 W/L for 30 min before each analytical test. 200 μL EXO@PL + Ca + SA and EXO were collected and placed on a copper mesh for 20 min. Subsequently, the supernatant was removed, and the sample on the copper mesh was treated with a phosphotungstic acid staining solution. Finally, the sample was allowed to stand for 10 min before being positioned at room temperature for Transmission electron microscope (HT7800, Hitachi High-Tech Company, Beijing, China) observation. In addition, a total of 20 μL of EXO samples were transferred to a new 1.5 mL EP tube, and 980 μL Dulbecco's phosphate-buffered saline (DPBS) was subsequently added. Particle diameter and quantity of exosomes in both the EXO and EXO@PL + Ca + SA samples were subsequently analyzed using Nanoparticle Tracking Analysis (NTA) (DKSH (Shanghai) Co., Ltd., China). Protein concentration of exosomes was measured using the BCA protein concentration kit, followed by Western Blotting analysis of the marker

proteins CD9, CD63, ALIX, and TSG101 [24].

2.6.9. Exosomes hydrogel storage time

Lyophilized hydrogel powder (5 g) was transferred into a sealed 50 mL centrifuge tube and stored at room temperature under dry conditions [24]. The total exosome particle count was quantified at days 0, 7, 14, 21, 28, and 35. The storage performance of the EXO@PL + Ca + SA hydrogel was evaluated by calculating the exosome retention rate (particles $_{day\ n}$/particles $_{day\ 0}$) over time.

2.6.10. Release and degradation of EXO@PL + Ca + SA

PKH26 staining solution was combined with exosomes at a ratio of 1:100 and incubated at 37 °C for 30 min. Subsequently, the preparation of the EXO@PL + Ca + SA hydrogel was conducted. The exosome labeling group served as the control. Fluorescence intensity was measured using a microplate reader, with excitation at 545 nm and emission at 586 nm, on days 0, 2, 4, 6, and 8. Furthermore, the release kinetics of the hydrogel was examined by fitting to common release models, including the Zero-order model: Mt./M∞ = kt, First-order model: 1- Mt./M∞ = e-kt, and Higuchi model: Mt./M∞ = kt1/2. In these equations, Mt., M∞, k, and n denote the released exosome at time t, the equilibrium, the release rate constant, and the release index, respectively [30]. The aim was to identify the best-fitting curve for the data. The release rate was calculated using the following formula.

$$\text{Release rate}\ (\%) = \frac{F_t}{F_0} \times 100\%$$

where F_t: the fluorescence intensity of daily; F_0: the total fluorescence intensity.

The degradation rate was utilized to represent the degradation of exosome hydrogels. A volume of 1 mL of freeze-dried exosome hydrogel was placed into a six-well plate containing 3 mL PBS. The samples were removed out every day for freeze-drying and weighing for a total of one week. The degradation rate (%) was calculated using the following formula.

$$\text{Degradation rate}\ (\%) = 1 - \frac{D_t}{D_0} \times 100\%$$

where D_t: the weight of hydrogels daily; D_0: the total weight of hydrogels.

2.7. The effect of EXO@PL + Ca + SA hydrogels on cells

2.7.1. EdU assay

The potential cytotoxicity of the hydrogel on cells was assessed using EdU staining [31]. The hydrogel was mixed with the culture medium (1:50 *v*/v) and added to the culture flask simultaneously with the cells. The EdU fluorescence intensity of the cells was observed using a fluorescence microscope (MF-52-N, Guangzhou Mingmei Optical Technology Co., Ltd., Guangdong, China) at 6 and 12 h.

2.7.2. Cell activity

The cell activity was observed by AO stain; meanwhile, ROS content was assessed to determine the effect of the hydrogel on the functional activity of fibroblasts. In addition, the exosomes' controlled release rate in the hydrogel was assessed by F-actin stain. In this experiment, fibroblasts (Fbs) were treated with PL + Ca + SA, EXO, and EXO@PL + Ca + SA, and AO and ROS reagents were added after 48 h of co-culture, respectively. Half an hour later, the fibroblasts' fluorescence was observed using a fluorescence microscope (MF52-N + MSX2; China). Notably, the initial cell density in the F-actin group was set at 4×10^4 cells/mL, which was half the density used in the other groups. F-actin staining was performed on days 3 and 7 to provide a more accurate evaluation of the exosome release rate. Following cell culture, radiographic imaging was performed, and immunofluorescence staining was employed for quantitative protein analysis [32].

2.7.3. Transcriptome analysis of fibroblasts treated with EXO@PL + Ca + SA hydrogel

Fibroblasts cultured in each group (with ≥3 biological replicates in each group) were collected following treatment with the hydrogel [33]. Total RNA was extracted using TRIzol or commercial kits, and the concentration and purity were determined by NanoDrop. Then, double-ended sequencing was performed via the Illumina platform. After quality control analysis of the original sequencing data, the gene expression levels were statistically analyzed. Differential expression analysis was performed using DESeq2/edgeR (screening threshold log2FC ≥1 and FDR < 0.05), and PCA, sample correlation/distance heatmaps were used to show the segregation and repeatability consistency between groups for the differential genes. Subsequently, functional enrichment analyses were carried out, including Gene Ontology (GO), Kyoto Encyclopedia of Genes and Genomes (KEGG) and Reactome (FDR < 0.05), and Gene Set EnrichmentAnalysis (GSEA) was used to evaluate the overall changes of the pathway based on the whole gene sequencing list. Meanwhile, the differential genes were imported into STRING to construct the PPI network and visualized in Cytoscape to identify the key hub genes and functional modules. The raw transcriptome sequencing data are deposited in the National Center for Biotechnology Information (NCBI) Sequence Read Archive (accession number PRJNA1426483; https://www.ncbi.nlm.nih.gov/, accessed 22 February 2026).

2.8. Histopathology and immunohistochemistry on mouse wound tissue

C57BL/6 mice were euthanized on postoperative days 7 and 14. Wound and surrounding tissue samples were collected and processed into paraffin-embedded sections for hematoxylin and eosin (H&E), Masson's trichrome staining, and immunofluorescence analyses targeting ROS, CK14, CK19, COL—I, COL-III and α-SMA [34]. Wound diameter was measured from H&E slices and quantified using K-Viewer software.

2.9. Statistical analysis

Statistical analysis was performed using GraphPad Prism software, version 10.2.3. All data were presented as means ± standard deviations (SDs). A *t*-test was used to analyze differences between groups. A two-way analysis of variance (ANOVA) test was used to assess the statistical significance of the mean values of more than two groups. A *p*-value less than 0.05 was considered statistically significant. 3D model images were drawn using the Figdraw online platform (https://www.figdraw.com/static/index.html#/), with the authorization code being ID: IWIYI93424, PPAAR3e454.

3. Results and discussion

3.1. Characterization of PL + Ca + SA hydrogels

A full characterization of the PL + Ca + SA hydrogels was conducted to understand the behavior of this material. PL + Ca + SA and SA + Ca hydrogels presented as white hydrogel blocks easily seen by the naked eye (Fig. 2A), whereas the other groups did not show this macroscopic character. These differences are attributable to the ability of sodium alginate (SA) and calcium ions (Ca) to create a three-dimensional, cross-linked network structure, which imparts mechanical/structural strength [35]. Meanwhile, the structural density and thickness of the PL + Ca + SA hydrogel decreased because carbonyl (CO) groups from PL replace some of the carboxyl (COO) groups of SA in its binding to Ca, which ultimately reduces the mechanical strength provided by the SA + Ca interaction. The structural edges (Fig. 2D) of the two groups of hydrogels (PL + Ca + SA and SA + Ca) were clear. However, the microscopic morphology of the PL + Ca and PL + SA groups revealed gel-like

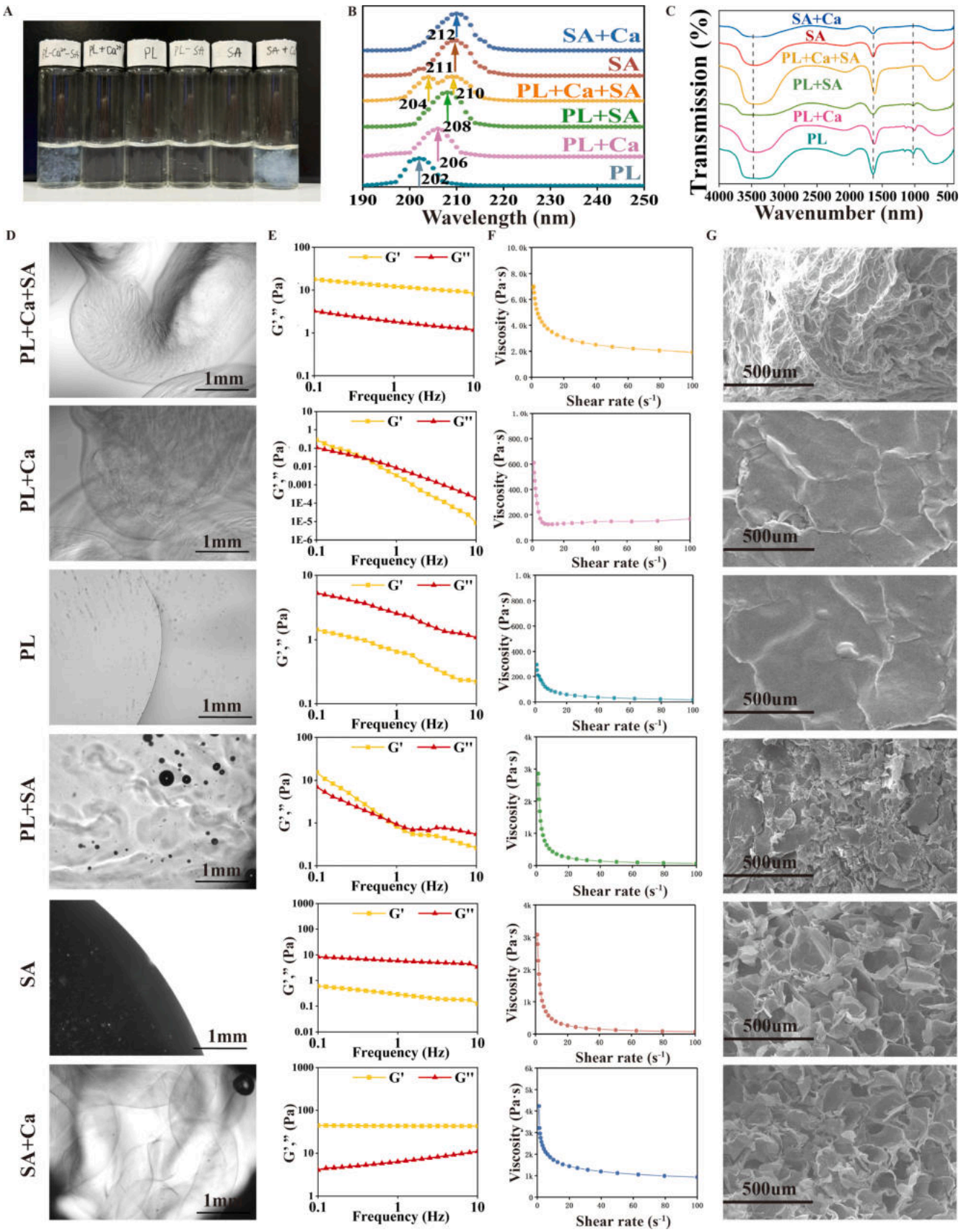

Fig. 2. Preparation and structural changes of hydrogels. A. Photos of PL + Ca + SA hydrogel preparation. Characterization of hydrogel by Ultraviolet spectroscopy B, Fourier transform infrared spectroscopy (FTIR) C, Photographs observed under a microscope D, Rheological frequency-sweep curves E, Viscosity curve F, and SEM of hydrogel G.

structures, wavy and with unclear edges, while being transparent in color and soft in texture. This behavior can be attributed to the instability of their fluid structure, which obstructs accurate light refraction [36]. It also indicates that PL can form unstable weak ionic bonds with other single components [37].

Ultraviolet full-wavelength absorption spectroscopy is a valuable tool for evaluating intermolecular interactions by analyzing variations in displacement and absorbance intensity [38]. The ultraviolet spectra of the different hydrogels are shown in Fig. 2B. The maximum absorption wavelengths of the PL, PL + Ca, PL+ SA, SA, SA + Ca and PL + Ca + SA groups appeared between 200 and 215 nm, with the absorption peak of PL observed near 202 nm. Notably, PL structures (PL + Ca + SA, PL + SA, PL + Ca) exhibit a redshift (long-wavelength shift) compared to PL, indicating that charge transfer occurs between the substances, leading to a conjugation effect and the formation of a new chemical bond [39]. Similarly, SA + Ca also showed a modest redshift in maximum absorption wavelength compared to free SA (211 → 212 nm). However, when compared to SA, the PL + SA complex shows a blue shift (towards lower wavelengths), suggesting a disruption of molecular planarity and a stacking effect between both polymers [40]. In conclusion, the ultraviolet spectrum of the hydrogel indicates that PL cannot directly form a stable cross-linked structure with SA. However, the introduction of calcium ions modifies the interactions between the two polymers, thereby facilitating the development of a novel chemical structure. Further FTIR analysis (Fig. 2C) shows that calcium ions can form ionic bonds with PL and SA, respectively. The characteristic absorption bands of PL were observed at 3200–3600 and 1000–1150 cm^{-1} corresponding to functional groups -OH, and C-O-C/C-O (characteristic peaks of sugar rings and glycosidic bonds), respectively [41]. Similarly, the SA spectrum showed -COO^- stretching vibrations at 1600 cm^{-1} and -OH stretching vibrations at 3200–3600 cm^{-1}, same as PL, respectively. In the SA + Ca system, the shift of the asymmetric stretching vibration peak of alginate's -COO^- group from 1600 cm^{-1} to approximately 1580 cm^{-1} confirms the successful formation of the SA-Ca ionically crosslinked network. In addition, shifts in the characteristic C-O-C/C-O groups were observed in the PL + Ca system, indicating its ability to form a network. In the PL + Ca + SA double-network system, the presence of characteristic peaks indicative of SA + Ca crosslinking was reaffirmed. Moreover, the hydroxyl stretching region (3200–3600 cm^{-1}) displayed a marked broadening and a clear shift. Furthermore, the position of the alginate -COO^- peak showed subtle yet distinct changes compared to the singular SA + Ca network. Collectively, these results indicate that pullulan chains are forming strong hydrogen bonding interactions with the sodium alginate-calcium ion network. This leads to a tight integration and mutual interpenetration of the components, resulting in a synergistically stable double-network hydrogel structure.

Shear modulus and viscosity analyses were performed on the hydrogels to gain a deeper understanding of their rheological characteristics. As illustrated in Fig. 2E and F, the energy storage modulus (G') of the SA + Ca and PL + Ca + SA groups significantly exceeds their loss modulus (G'). This indicates that the elastic properties of these two components are superior to their viscous properties, classifying them as solid-like components [42]. The G' of the PL + SA and PL + Ca structures initially increased and subsequently decreased, indicating that with increasing shear frequency, the elasticity of the substance diminished while its viscosity increased, leading to a transition of the structure from solid to liquid. This observation aligns with prior findings regarding the apparent structure. Although PL contains multiple hydroxyl groups, the ionic bonds formed with Ca and SA are susceptible to disruption by environmental factors, consequently resulting in an unstable hydrogel structure. Meanwhile, when the G" of a single component exceeds the G', the viscosity of the substance surpasses its elasticity, indicating a liquid state. The shear modulus reflects the internal structural state of a material, whereas viscosity pertains to its thermal decomposability [43]. As the temperature increases, the viscosity of the hydrogel gradually diminishes. This phenomenon can be attributed to the fact that elevated temperatures accelerate molecular motion, causing the hydrogel chains to become more flexible [44].

The morphology of the freeze-dried PL and PL + Ca hydrogels (Fig. 2G) was flaky with no evident protruding structures. Although the SA and SA + Ca groups contained hollow structures, their strong mechanical support made them susceptible to breakage during the freeze-drying process, resulting in the formation of a significant number of fragments, which adversely affected the stability of the internal active substances. In contrast, the PL + Ca + SA group effectively mitigated this issue. This supports the proposed application of the PL + Ca + SA group for the isolation, stabilization, and release of exosomes.

3.2. The influence of ultrasonic treatment on the structure of hydrogels

The critical advantage of hydrogel-based isolation for exosomes lies in its ability to efficiently remove excess water from the culture medium while preserving exosomal structural integrity [45]. A schematic diagram illustrating the freeze-dried storage process and the subsequent ultrasonic-assisted reconstitution of the EXO@PL + Ca + SA hydrogel is shown in Fig. 3A. Fig. 3B illustrates the quantity of water evaporated during freeze-drying for various components. Among all tested formulations, the SA + Ca hydrogel exhibited the least water evaporation, which is likely attributable to its robust and densely crosslinked structure that significantly retards water removal [46]. The incorporation of PL mitigates the shrinkage of SA + Ca and enhances the removal of free water. Consequently, the SA + Ca hydrogel alone is not suitable for exosome isolation because its poor dehydration characteristics could negatively affect process efficiency. The freeze-dried EXO@PL + Ca + SA hydrogel powder was stored in a sealed container at room temperature, and exosome particle concentrations were measured at defined intervals to assess the hydrogel's capacity to enhance exosome storage stability (Fig. 3C). The results showed that after 35 days of storage, more than 90% of the exosome particles were retained within the hydrogel. After 90 days of storage, the hydrogel retained 50% of its exosomes. This result indicates that the hydrogel significantly enhances exosome stability and industrialization potential under ambient conditions compared to the EXO group. Although the double-layer hydrogel improves storage of exosomes, its structural configuration inherently restricts exosome release. To ameliorate this limitation, ultrasonic-assisted dissolution was employed to facilitate the cleavage of the sodium alginate and calcium ion bonds within the hydrogel. This approach not only aids in the reconstruction of the hydrogel structure but also enables a controlled release of exosomes. Ultrasonic waves at a specific intensity can break molecular bonds and thus facilitate the release of internal active compounds [47]. In addition, the ζ potential is an important indicator for evaluating the stability of a colloidal dispersion. The colloidal stability, governed by electrostatic repulsion, is directly correlated with the absolute ζ potential [48]. After ultrasonic treatment of EXO@PL + Ca + SA hydrogel at different intensities, the ζ potential showed significant differences (Fig. 3D). The absolute ζ potential decreased with increasing ultrasonic power, signifying a reduction in stability. The value reached a minimum at 600 W/L, at which point the colloidal structure was entirely disrupted. Notably, after treatment at 400 W/L, the system's absolute ζ potential approached that of the PL + Ca benchmark. This suggests that moderate ultrasonication selectively cleaves the ionic bonds within the SA-Ca network without inducing a complete structural collapse of the hydrogel [49].

Meanwhile, following the ultrasonic redissolution of the freeze-dried PL + Ca + SA hydrogel structure, G" was significantly higher than G' (Fig. 3F–G), and the solution transitioned into a high-viscosity liquid. The ultrasonic treatment induced a transformation from solid to liquid, indicating that this treatment facilitates the disruption of the robust ionic bonds between SA and Ca. The ultraviolet spectra of the hydrogel before and after ultrasonic treatment are presented in Fig. 3E. The characteristic absorption peak of SA + Ca at 210 nm disappeared after ultrasonic treatment. In contrast, the absorption peak associated with PL

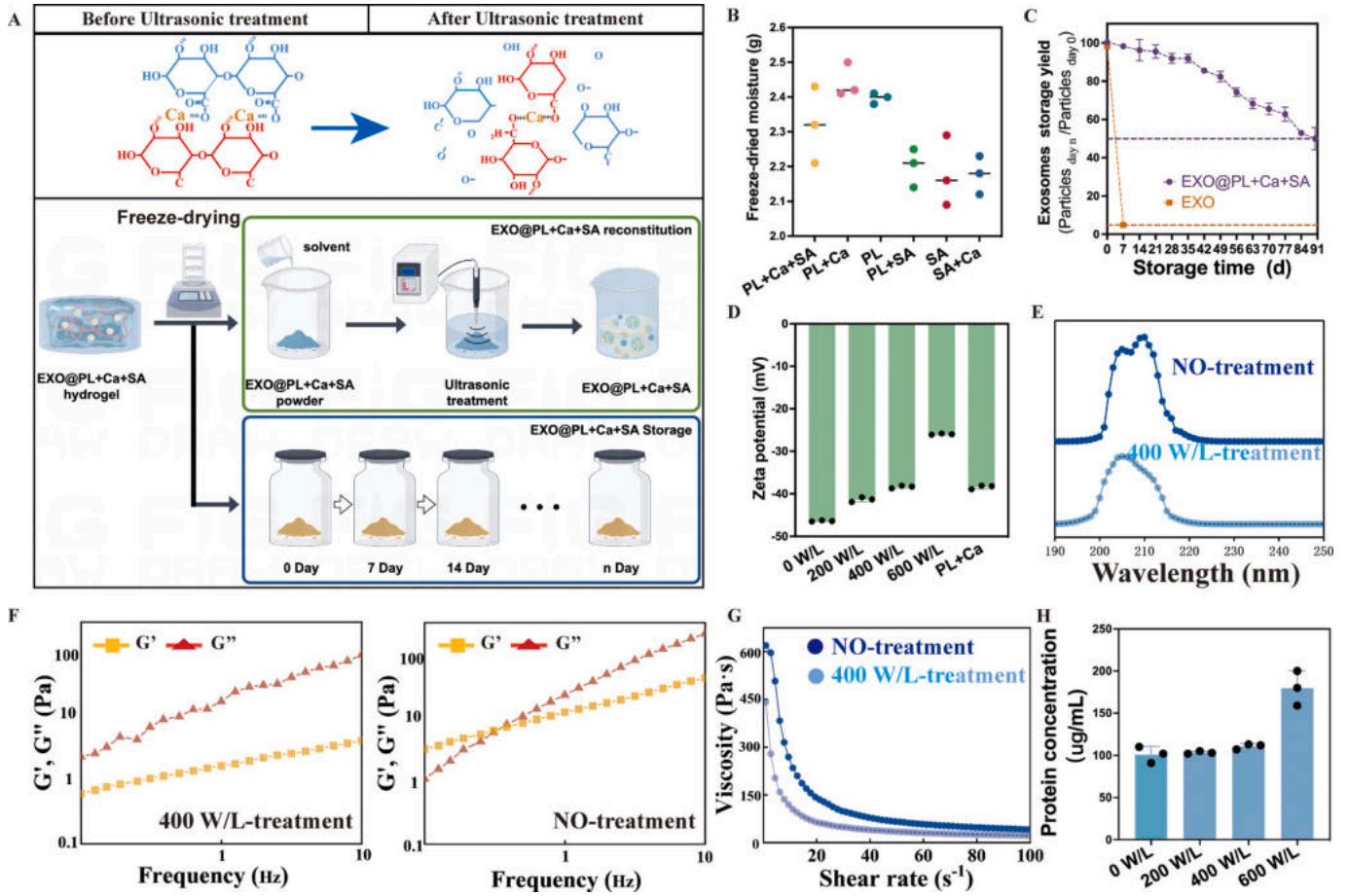

Fig. 3. Ultrasonic-assisted dissolution of hydrogels achieves the effect of controlled release. A. Schematic diagram of the lyophilized storage and ultrasonic treatment on the structure of hydrogels. B. The statistical analysis of the moisture loss in freeze-dried hydrogels. C. The exosomes storage yield at different storage times. D. The zeta potential of different ultrasonic power treatment hydrogels. Effect of ultrasonic treatment on rheological frequency-sweep curves (F) and viscosity (G) characteristics of PL + Ca + SA hydrogel lyophilized powder after reconstitution. E. Ultraviolet spectroscopy of PL + Ca + SA hydrogel after ultrasonic treatment. H. The protein concentrations of EXO@PL + Ca + SA hydrogels after different ultrasonic treatments.

(~205 nm) broadened. Although the ionic bonds pertaining to PL remained, the intermolecular interactions of SA + Ca were significantly reduced. In addition, the retention of exosome membrane integrity after different ultrasonic treatments was evaluated by measuring the protein concentration of the hydrogels (Fig. 3H). The results showed that ultrasonic treatment at 600 W/L significantly increased the protein concentration of the hydrogels, which may be attributed to exosome membrane rupture and subsequent protein leakage caused by excessive ultrasonic exposure. Thus, these findings indicate that the ultrasonic-assisted dissolution technique has the potential to significantly enhance the release of active compounds from the PL + Ca + SA hydrogel by disrupting its molecular structure.

3.3. Characterization, isolation and release rate of EXO@PL + Ca + SA hydrogel

The process of isolating exosomes with PL + Ca + SA is illustrated in Fig. 1A–B. Transmission electron microscopy (TEM) analysis of the EXO@PL + Ca + SA hydrogel (Fig. 4A) revealed distinct vesicular particles. Exosomal marker proteins, including ALIX, CD63, TSG101, and CD9, demonstrated clear bands (Fig. 4B–C) after isolation with PL + Ca + SA. Statistical analysis revealed that ALIX and TSG101 levels were significantly higher in the EXO group compared to EXO@PL + Ca + SA, whereas CD63 and CD9 showed no significant differences. This difference may be attributed to the obstruction of macromolecular proteins by hydrogels. Particle size analysis of the EXO@PL + Ca + SA showed particles significantly larger than typical exosomes, which may be attributed to the presence of SA fragments and the formation of small particle complexes of PL-exosomes resulting from ultrasonic disruption.

To further characterize exosomes loaded hydrogels, the ultraviolet absorption peak spectra of EXO@PL + Ca + SA are shown in Fig. 4J. Sharp peaks appear in the exosomes sample (without hydrogel) between 260 and 280, mainly due to the presence of various proteins and nucleic acids in exosomes [50]. In contrast, a sharp peak appears in EXO@PL + Ca + SA near 240 nm, indicating that the hydrogel is wrapped outside the exosome, reducing the absorption peak of the exosome. Furthermore, to delineate the specific localization of exosomes (encapsulated within the hydrogel matrix versus adsorbed on its surface), a control sample (EXO + PL + Ca + SA) was prepared by introducing exosomes to the pre-formed hydrogel. EXO + PL + Ca + SA showed significant spectral differences compared to EXO@PL + Ca + SA, with a wider range of characteristic peak positions (same as EXO). These findings further support that the exosomes were encapsulated within the hydrogel and not simply adsorbed to the hydrogel surface.

The efficiency of exosome isolation using the proposed hydrogel strategy was evaluated by quantifying the total number of exosome particles within the hydrogel. Nanoparticle tracking analysis (NTA) results (Figs. 4D–E, S2A) showed no significant difference in the total number of isolated exosome particles between the reconstituted EXO@PL + Ca + SA and exosomes obtained via ultracentrifugation (UC). The incorporation of PL and SA resulted in a marginally higher particle count in the hydrogel compared to ultracentrifugation.

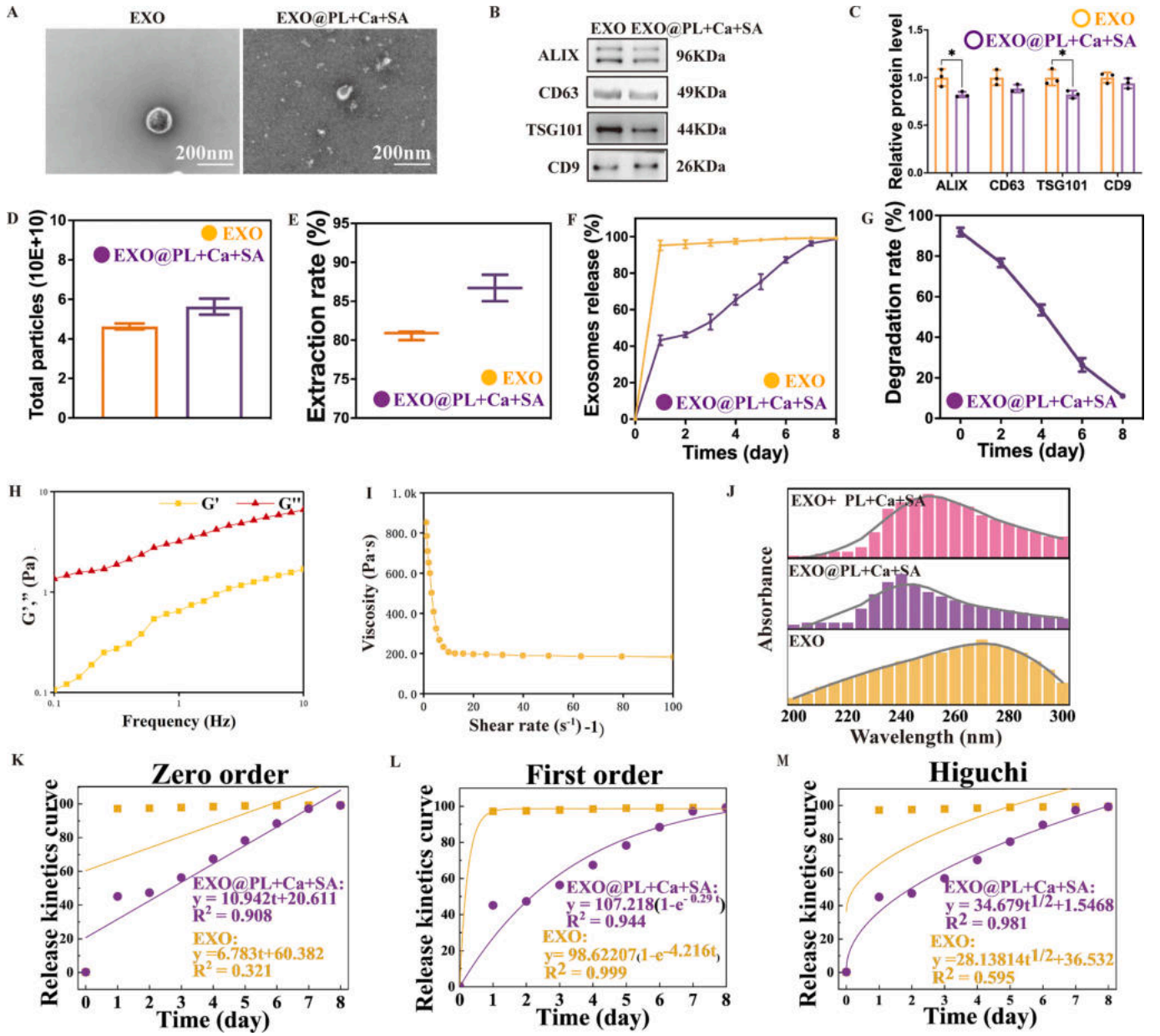

Fig. 4. EXO@PL + Ca + SA hydrogel lsolation effect and release rate. Exosomes characterization by TEM (A), Western blot (B), and Statistical analysis of Western blot (C). The total particles of EXO and EXO@PL + Ca + SA (D), and isolation rate (E). F. Exosomes release rate of EXO@ PL + Ca + SA hydrogel. G. Degradation rate of EXO@ PL + Ca + SA hydrogel. Rheological frequency-sweep curves (H), and Viscosity curve (I) of EXO@PL + Ca + SA. J. EXO@PL + Ca + SA hydrogel loading of exosomes UV spectroscopy. The Zero order (K), First order (L) and Higuchi (M) release kinetics fitting curve of the hydrogel.

Additionally, comparison of protein concentrations between the EXO and EXO@PL + Ca + SA hydrogel groups (Fig. S2B) revealed a slightly higher protein concentration in the EXO@PL + Ca + SA hydrogels; however, this difference was not statistically significant. It further indicates that after the isolation of exosomes by hydrogel, the impurity level is very low, suggesting that the proposed in-situ hydrogel formation method for the isolation of exosomes is a promising industrial isolation approach. Furthermore, the shear modulus (Fig. 4H) and viscosity (Fig. 4I) remained unchanged after the reconstitution of EXO@PL + Ca + SA, indicating that the presence of exosomes did not influence these parameters. This observation is consistent with the results obtained for PL + Ca + SA. Based on the liquid properties of the hydrogel, the amount of released exosomes from the hydrogel was calculated by detecting the fluorescence of labeled exosomes at different time periods (Fig. 4F). Compared with EXO (without hydrogel), those encapsulated in the hydrogel exhibited a characteristic slow release, with complete release occurring by after a week. Additionally, the structural integrity of the hydrogel also exhibited degradation over time (Fig. 4G); by the eighth day, it constituted only 11.6% of its original mass. Furthermore, analysis of the release kinetics fitting curve using mathematical models indicates that neither group exhibited a constant-speed diffusion state (Fig. 4K–M). The EXO group showed a good agreement with first-order diffusion, suggesting a strong correlation between the release rate and the remaining concentration of EXO, as expected. In contrast, the EXO@PL + Ca + SA group displayed characteristics better aligned with Higuchi diffusion, which implies that the release is primarily controlled by diffusion and follows typical Fickean behavior [51]. Therefore, it can be concluded that the hydrogel significantly enhances the isolation, stability and release of the exosomes, thereby facilitating their application.

3.4. Effects of EXO@PL + Ca + SA on proliferation, migration and performance of mouse fibroblasts

hUC-MSCs have the characteristics of low immunogenicity and strong amplification ability. The exosomes secreted by them have been widely proved to be able to regulate inflammatory responses and promote signal pathways related to tissue regeneration. Fibroblasts are the main functional cells in wound healing. To assess the performance and cytotoxicity evaluation of the material, EXO@PL + Ca + SA was co-cultured with mouse skin fibroblasts for 24 h. Following this culture

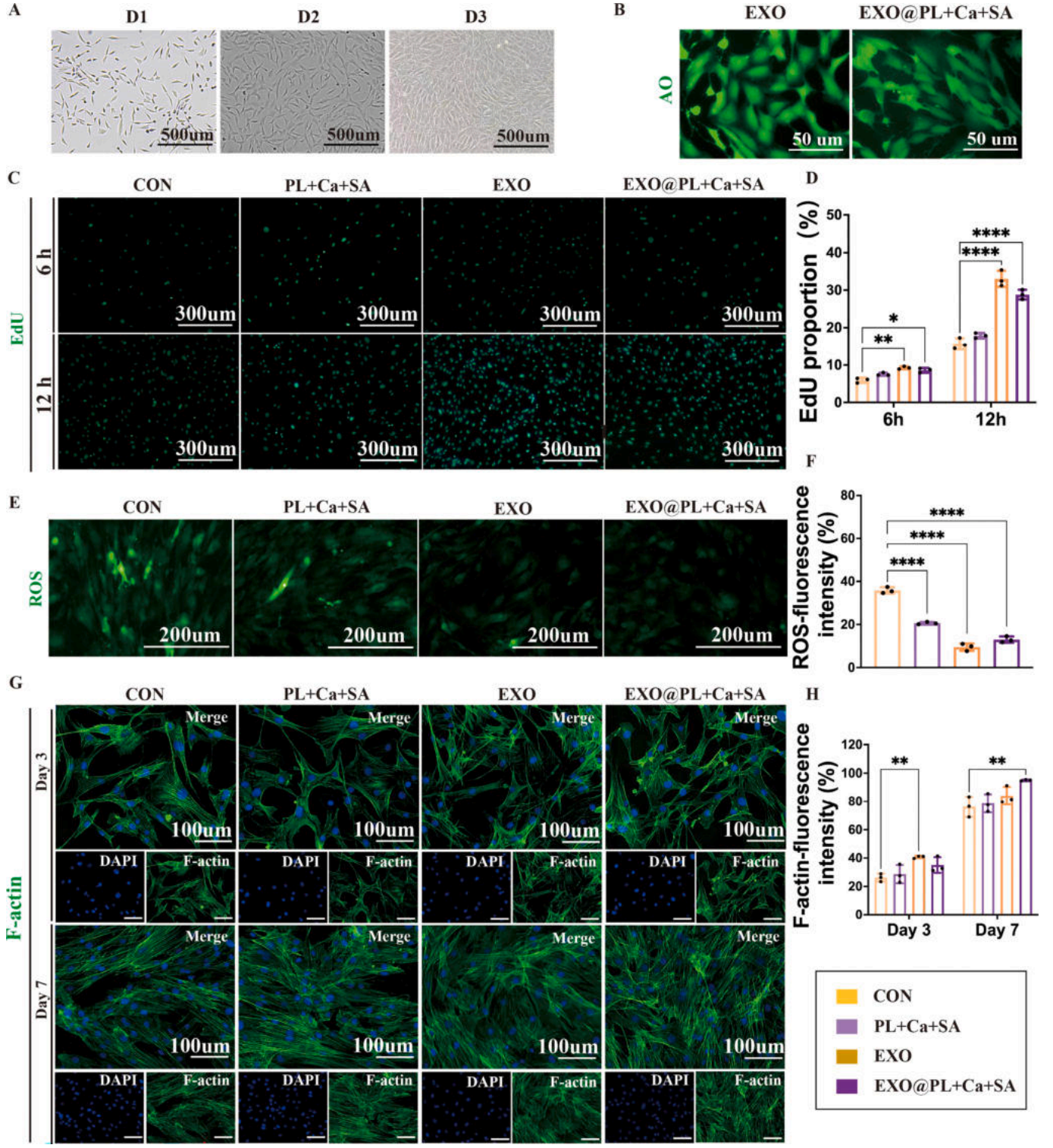

Fig. 5. Effects of EXO@PL + Ca + SA hydrogel on proliferation, migration and bio-performance of mouse fibroblasts. A. Growth morphology of fibroblasts. B. The live cell stain of fibroblasts by EXO@PL + Ca + SA hydrogel treatment. C. The effect of different treatments on the proliferation (EdU) of fibroblasts. D. Statistical analysis of EdU proliferation rate. E. ROS formation of fibroblasts treated by EXO@PL + Ca + SA. F. Statistical analysis of ROS production. G. F-actin formation of fibroblasts treated by EXO@PL + Ca + SA at day 3 and day 7. H. Statistical analysis of F-actin production. Data represented is as mean ± SD; ns, no significance, *$p < 0.05$, **$p < 0.01$, ***$p < 0.001$, ****$p < 0.0001$.

period, the exosomes released from the hydrogel were observed in culture. Subsequently, the labeled fluorescent exosomes were detected, and the results are shown in Fig. S4A-B. A clear incubation time-dependent in intracellular fluorescence was recorded. Fig. 5A shows the phenotypical changes of cells at different times after EXO@PL + Ca + SA treatment. The findings indicate that EXO@PL + Ca + SA does not exhibit toxic effects on the cells, and the overall cell growth state is favorable. Fig. 5B shows that there is no significant difference in cell viability between the EXO and EXO@PL + Ca + SA groups and demonstrates the safety of the PL + Ca + SA hydrogel. The proliferative activity of EXO@PL + Ca + SA on fibroblasts is shown in Fig. 5C–D. The EdU intensity observed in the EXO and EXO@PL + Ca + SA groups was significantly higher compared to the other two control groups, with no significant differences noted between these two groups at 12 h.

Furthermore, the mitochondrial metabolic function, as indicated by reactive oxygen species (ROS) production, served as a measure of the proliferative activity of the cells (Fig. 5E–F). The findings indicate that, in comparison with the untreated control (CON), EXO@PL + Ca + SA was able to regulate mitochondrial function, stabilize the mitochondrial respiratory chain, enhance metabolic function, and consequently reduce ROS production [52]. When mitochondrial function is optimized, an adequate supply of ATP is ensured, enabling fibroblasts (Fbs) to efficiently synthesize and secrete collagen, thereby maintaining the normal structure and function of the extracellular matrix [53]. Actin microfilaments (F-actin) are capable of forming actin fibers under ATP supply [54]. These fibers, in addition to providing contractility to tissues, serve as intracellular tracks for material transport and organelle positioning, representing a hallmark of integrated cellular activity [55]. The levels of F-actin (Fig. 5G–H) in the EXO group were significantly higher than those observed in the control (CON) group at day 3. In addition, only the EXO@PL + Ca + SA group fluorescence was significantly higher than the control group at day 7. This is consistent with a sustained release of exosomes from the hydrogel, which induces a prolonged positive effect on the cells. In addition, the scratch assay demonstrated that continuous exosome release from the hydrogel significantly accelerated fibroblast migration (Fig. S4C), leading to a higher scratch closure rate than the EXO group alone, with a notable increase within 24 h. Consequently, the results obtained demonstrate that the EXO@PL + Ca + SA exhibits no cytotoxic effects on cells, while significantly enhancing the proliferation, migration, and overall bio-performance of mouse fibroblasts.

3.5. *EXO@PL + Ca + SA hydrogel effectively promotes rapid wound healing in mice*

Promoting efficient healing of acute wounds represents one of the most effective strategies for preventing the development of hypertrophic scars. The acute wound model in mice is a classic animal model for studying the mechanism of skin injury repair and evaluating the efficacy of regenerative materials. This model can stably simulate the complete healing process of a wound from the inflammatory phase, proliferative phase to the remodeling phase, and is therefore widely used to analyze key biological events such as changes in cell behavior, collagen deposition and inflammatory regulation. In this context, we conducted an investigation utilizing EXO@PL + Ca + SA hydrogel to facilitate rapid wound healing in a murine model. The sustained-release effect of EXO@PL + Ca + SA on murine wounds, as well as its therapeutic efficacy in accelerating acute wound healing in mice, is demonstrated in Fig. 6A. The wounds in the animals treated with control EXO and EXO@PL + Ca + SA healed more rapidly, with nearly imperceptible scarring observed at 14 days when compared to the control (CON) group (Fig. 6B–C). Additionally, tissue samples from the wounds 14 days after generation were collected for histological examination using H&E and Masson's trichrome staining to assess the recovery of subcutaneous tissue. The architecture of skin appendages, such as hair follicles and sebaceous glands, signifies an absence of scarring during wound healing [56]. H&E staining in the EXO and EXO@PL + Ca + SA groups demonstrated the presence of hair follicle structures, which exhibited significant differences compared to those in the control (CON) group (Fig. 6D–E). Furthermore, the regenerated skin in the EXO@PL + Ca + SA group closely resembled the structure of normal skin compared with the EXO group, with a notable abundance of sebaceous glands. This improvement may be attributed to the sustained release of the hydrogel, which allows exosomes to continuously and effectively facilitate wound repair [57]. In addition to skin appendages, the subcutaneous tissue layer (extracellular matrix) is constructed through collagen regeneration and remodeling [58]. Fig. 6F–G illustrates the dense blue collagen fibers and red muscle fibers within the subcutaneous tissue. An excess of muscle fibers may influence the wound remodeling process and contribute to the development of hypertrophic scars [41]. Compared to the control group (CON), the muscle fiber content in the EXO@PL + Ca + SA group was 30.8%, which is advantageous for achieving a rapid and healthy wound healing process.

Overall, both EXO and EXO@PL + Ca + SA hydrogel demonstrate beneficial effects in promoting the healing of acute wounds. However, the EXO@PL + Ca + SA hydrogel exhibits sustained-release properties, which facilitate the regeneration of healed skin that closely resembles normal tissue. This is characterized by an increased presence of skin appendages and collagen, which aligns with previous research findings. For instance, Li et al. (2025) developed a dual dynamic network hydrogel for encapsulating adipose-derived stem cell exosomes [59], which can significantly promote wound healing and reduce scarring and enhance skin regeneration. Furthermore, Xu et al. (2025) found that treatment with 3D hydrogels could more effectively restore corneal morphology and function by using gelatin methacryloyl hydrogels to encapsulate exosomes [60]. Collectively, these findings underscore the remarkable effectiveness of hydrogels in the delivery and sustained release of exosomes, promoting advancements in wound healing methodologies.

Furthermore, immunofluorescence staining analysis was conducted to assess the levels of reactive oxygen species (ROS) (Fig. 7A), cytokeratin 14 (CK14) and cytokeratin 19 (CK19) (Fig. 7B), the collagen types I and III (COL-I and COL-III) (Fig. 7C) and α-SMA (Fig. 7D) in the tissue of healing wounds. This analysis aimed to elucidate the influence of exosomes on wound healing. The results demonstrate a notable decrease in ROS levels within the group treated with exosomes compared to the control group (Fig. 7E). During the inflammatory phase of wound healing, the continuous release of inflammatory signals by macrophages sustains immune cell activation, leading to prolonged elevation of ROS levels [61]. Excessive ROS production can negatively influence inflammatory responses, potentially leading to tissue damage and fibrosis [62]. CK14 expression remained unchanged (Fig. 7F), while CK19 increased significantly (Fig. 7G). CK14 predominantly marks basal keratinocytes, and its steady level suggests preservation of basal-layer homeostasis rather than excessive hyperproliferation [63]. The observed up-regulation of CK19, a marker commonly associated with epidermal progenitors and adnexal (hair follicle) stem cell populations, is consistent with enhanced recruitment of progenitor cells during re-epithelialization. Such progenitor-driven regeneration is known to favor restoration of epidermal architecture and appendage contribution. Additionally, the contents of COL-I (Fig. 7H) and COL-III (Fig. 7I) in the EXO@PL + Ca + SA group demonstrated significant differences compared to the control (CON) group. Specifically, COL-I content in the EXO and EXO@PL + Ca + SA groups was found to be 16.38% and 28.4% of that observed in the CON group, respectively. In terms of COL-III, the levels were 10.75 times and 5.48 times greater than those in the control group, respectively. COL-I is the main protein that forms hypertrophic scars; its overexpression can lead to abnormal wound healing if not balanced with the ratio of COL-III [64,65]. These findings suggest that exosomes play a critical role in significantly inhibiting the formation of COL-I while promoting the synthesis of COL-III. The COL-I/COL-III ratio (Fig. 7J) of EXO@PL + Ca + SA is 0.62, whereas that of the control group is 13.89, further suggesting that exosomes can regulate the

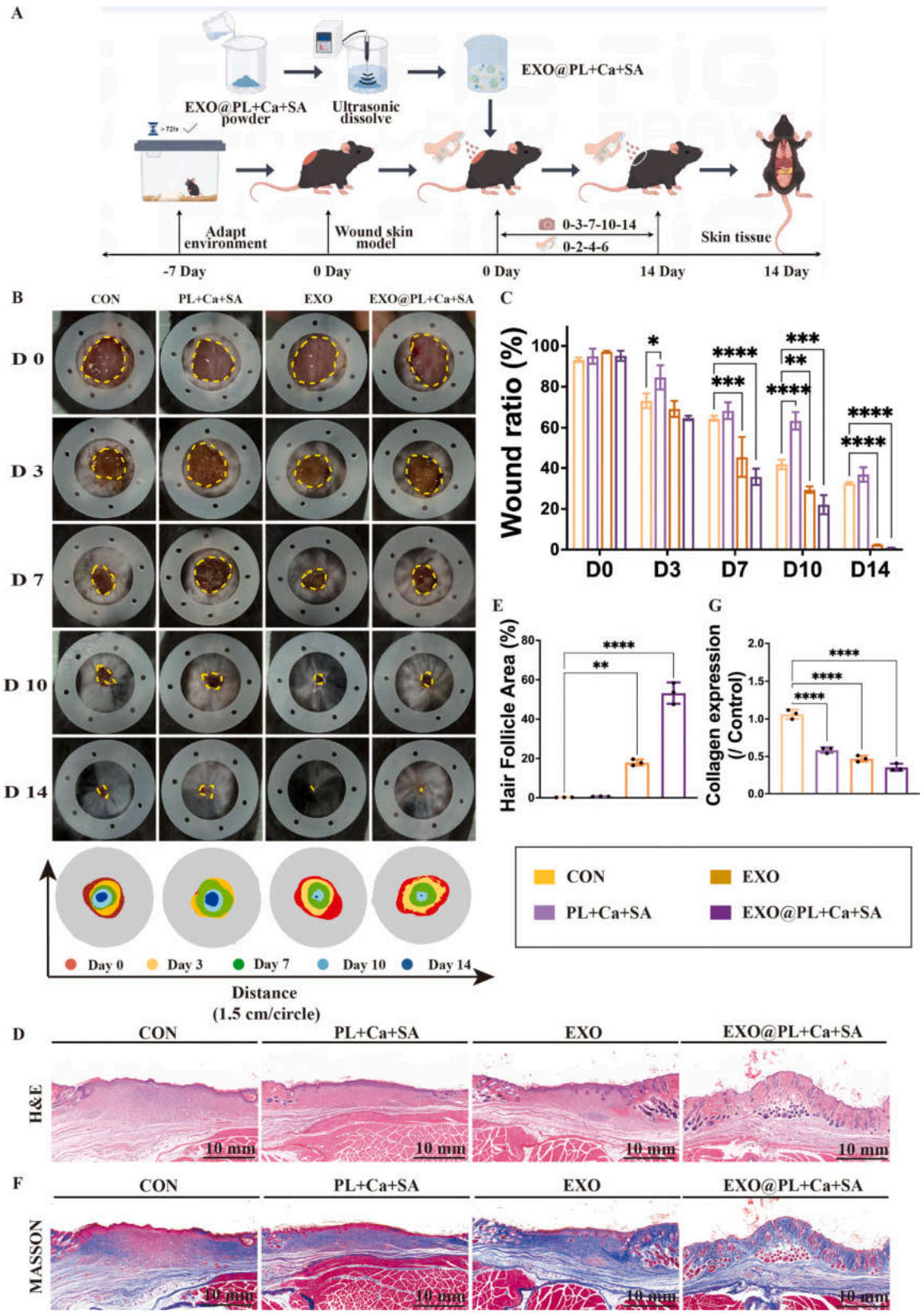

Fig. 6. EXO@PL + Ca + SA hydrogel effectively promotes rapid wound healing in mouse A. Schematic diagram of the mouse wound model treated by EXO@PL + Ca + SA hydrogel and the process of wound healing. B. Photographic records of wound recovery in mouse. C. Wound healing area statistics during wound recovery in mouse (compared with the control). D. H&E staining of mouse wound tissue. E. Hair follicle growth area of wound tissue at 14 days. F. Masson staining of mouse wound tissue. G. Collagen expression of wound tissue at 14 days. Data represented is as mean ± SD; ns, no significance, *p < 0.05, **p < 0.01, ***p < 0.001, ****p < 0.0001.

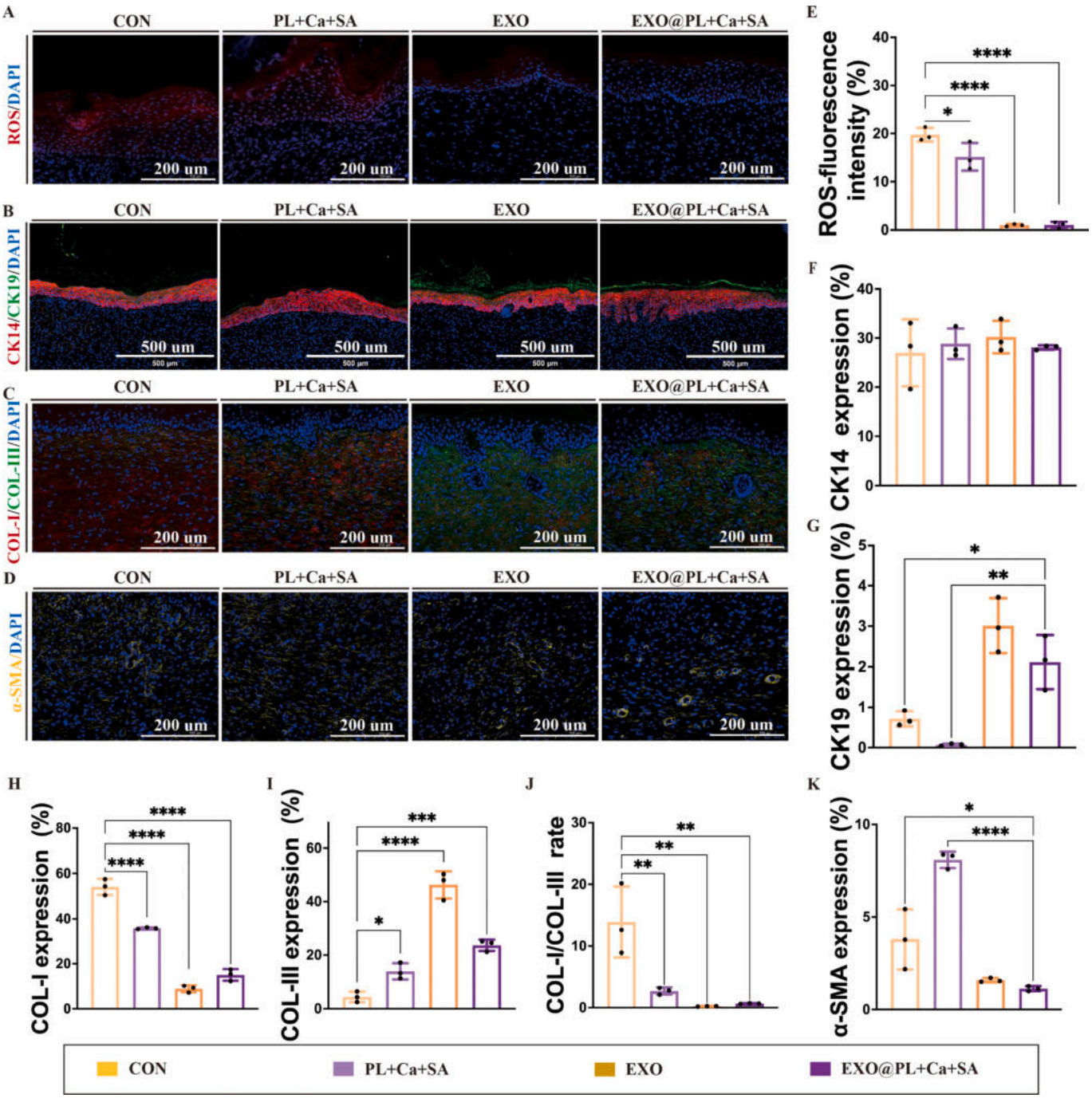

Fig. 7. Effect of EXO@PL + Ca + SA on ROS and collagen type staining (COL-I/COL-III) in mouse wound healing. A. ROS staining of mouse wound tissue. B. Immunofluorescence staining of CK14 and CK19 in mouse wound tissue. C. Immunofluorescence staining of COL-I and COL-III in mouse wound tissue. D. Immunofluorescence staining of α-SMA in mouse wound tissue. E-K. Statistical analysis of ROS, CK14, CK19, COL—I, COL-III, COL-I/COL-III fold change and α-SMA expression. Data represented is as mean ± SD; ns, not significance, *p < 0.05, **p < 0.01, ***p < 0.001, ****p < 0.0001.

proportion of collagen in wound healing.

COL-I is a key component of the fibrotic extracellular matrix (ECM) [66]. The inhibition of COL-I through the application of a hydrogel containing exosomes effectively diminishes the risk of ECM fibrosis and mitigates scar formation during the wound healing process. The content of COL-III in acute wounds of mice was increased by controlled release of exosomes from EXO@PL + Ca + SA hydrogel, and accelerated wound healing by replacing COL-I to form ECM. α-SMA is a critical marker protein associated with myofibroblasts, the primary cellular constituents responsible for the production of COL—I. These cells are activated from fibroblasts under specific conditions [67]. The levels of α-SMA in the hydrogel group were lower compared to the other groups (Fig. 7K), especially in the EXO group. This finding suggests that the sustained release of exosomes from hydrogels can diminish the population of myofibroblasts, thereby decreasing the synthesis of COL—I. Consequently, EXO@PL + Ca + SA hydrogel regulates the activation of myofibroblasts through controlled exosome release, modulates the COL-I to COL-III ratio during wound healing, and promotes recovery.

The beneficial effects of hydrogel treatment were confirmed through transcriptome analysis of mouse skin fibroblasts. Principal component analysis (PCA) (Fig. 8A) demonstrated a clear separation between the EXO group and the EXO@PL + Ca + SA group, reflecting strong

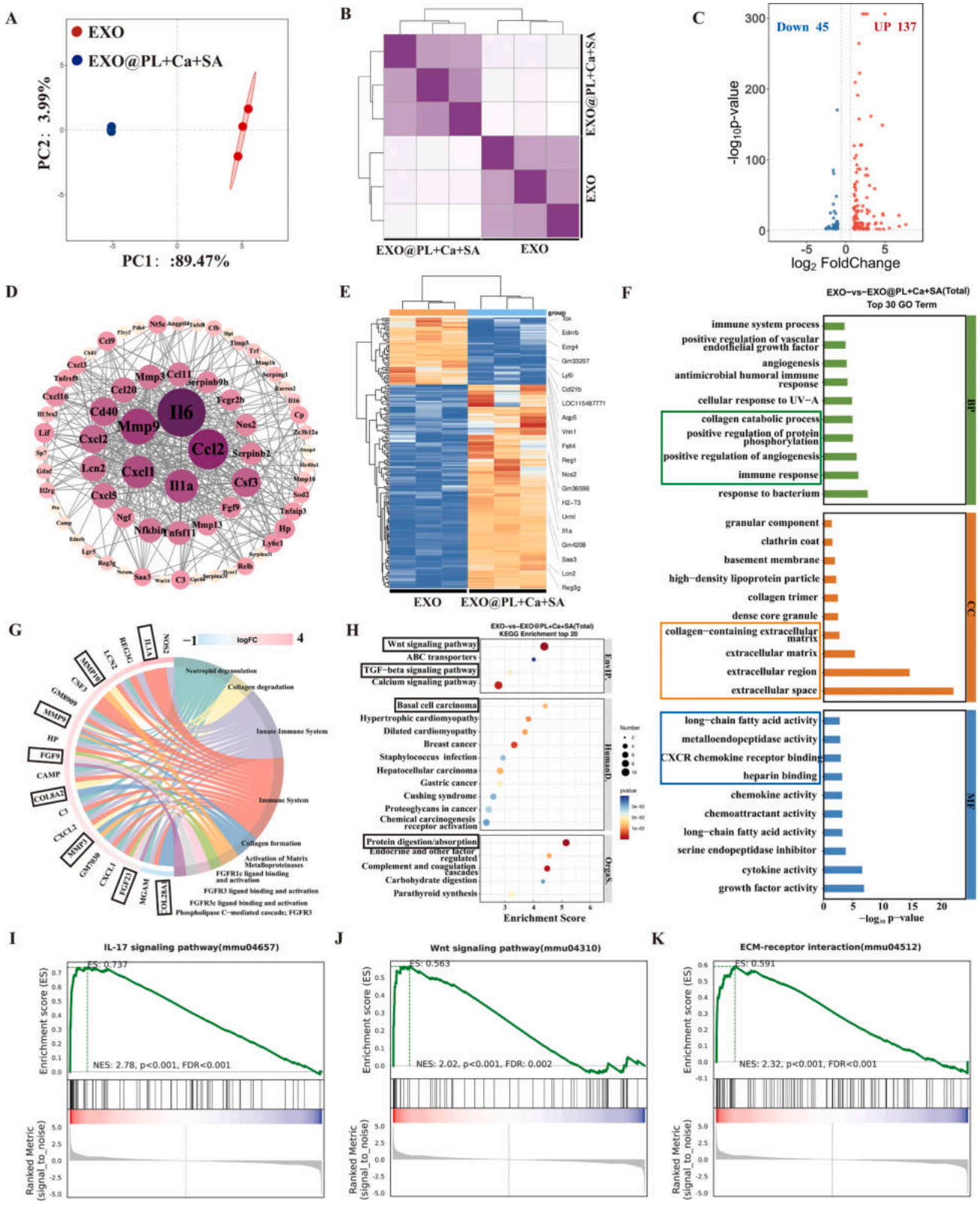

Fig. 8. Transcriptome analysis results of the effects of EXO@PL + Ca + SA treatment on fibroblasts. A. Principal component analysis (PCA) diagram showing the variance and standard deviation of the EXO and EXO@PL + Ca + SA datasets. B. Heat map of distances analysis between samples. C. Volcano plots displaying differential gene expression profile. D. Protein–protein interaction (PPI) network of differentially expressed genes. E. Heatmap of differentially expressed genes between the EXO and EXO@PL + Ca + SA groups. F. GO enrichment analysis of differentially expressed genes. G. Reactome enrichment analysis of differentially expressed genes. H. KEGG pathway enrichment analysis of differentially expressed genes. GSEA of IL-17 (I), Wnt (J) and ECM-receptor (K). Data represented is as mean ± SD; ns, not significance, *p < 0.05, **p < 0.01, ***p < 0.001, ****p < 0.0001.

reproducibility within each group. In addition, the heat map of the distances (Fig. 8B) between samples shows a high degree of similarity among biological replicates. Following hydrogel treatment, 182 genes (Fig. 8C) in fibroblasts exhibited significant differential expression. These genes formed an interaction network (Fig. 8D) centered on inflammatory factors, chemokines, and matrix remodeling, suggesting involvement in related biological processes or coordinated signaling pathways. Pro-inflammatory responses mediated by IL-6, IL-1α, and CSF3 mobilized CCL and CXCL chemokines, thereby enhancing immune regulation by macrophages and neutrophils [68,69]. In addition, reactive oxygen (ROS) related factors such as NOS2 and SOD2 accounted for observed changes in cellular inflammation [70]. Furthermore, Matrix metalloproteinase (MMP) family genes indicated extracellular matrix (ECM) degradation and promoted wound matrix remodeling [71]. Notably, inflammation-related genes in the hydrogel group were significantly upregulated in fibroblasts (Fig. 8E), suggesting that hydrogel treatment facilitates earlier entry into the inflammatory response, which may mobilize additional cells to combat infection and initiate early wound debridement [72]. Through gene enrichment statistics, it was found that GO enrichment (Fig. 8F), Reactome enrichment (Fig. 8G) and KEGG enrichment (Fig. 8H) were positively regulated in inflammation and ECM remodeling. Gene set enrichment analysis (GSEA) indicated significant positive enrichment of the IL-17 signaling pathway (Fig. 8I) in the experimental group, demonstrating activation of inflammation-related transcriptional programs. In addition, both the Wnt signaling pathway (Fig. 8J) and the ECM-related pathway (Fig. 8K) were activated. These findings align with the expected outcomes of acute wound healing in mice, as evidenced by the modulation of the ROS-associated inflammatory response, the extent of re-epithelialization (CK14/CK19), and ECM remodeling mediated by the regeneration of collagen subtypes. In summary, transcriptomic analysis indicated that hydrogel treatment promotes a more rapid initiation of the inflammatory response in fibroblasts compared with the exosome group, thereby regulating downstream wound-healing proteins and pathways.

4. Conclusion

In this study, a multifunctional pullulan/sodium alginate hydrogel was prepared for the isolation, stabilization and effective delivery of exosomes. Furthermore, the impact of the hydrogel-encapsulated exosomes on wound healing in a mouse model was examined. The PL + Ca + SA hydrogel effectively retained exosomes in cell culture medium and the number of exosome particles after isolation showed no significant difference from that by ultracentrifugation. Additionally, the double-layer grid hollow structure safeguards exosomes from quality loss during freeze-drying. When the exosome hydrogel solution was reconstituted, it showed a positive effect on promoting healing in mice. Overall, this research effectively integrates the processes of isolation, storage, and application of exosomes through the use of PL + Ca + SA hydrogels. This innovative approach significantly reduces the degradation of exosome quality and activity at various stages, thereby enhancing the operational efficiency of exosomes. Conclusively, this study offers a significant reference point for the industrial isolation of functional exosome products.

CRediT authorship contribution statement

Lihua Yang: Writing – review & editing, Writing – original draft, Investigation, Formal analysis, Data curation. **Cenlong Huang:** Visualization, Investigation. **Mingwei Shen:** Visualization, Formal analysis, Data curation. **Chenyu Xu:** Writing – review & editing, Visualization, Investigation. **Zonglin Guo:** Investigation, Formal analysis. **Juan Gallo:** Writing – review & editing, Data curation. **Meijin Guo:** Writing – review & editing, Supervision, Funding acquisition. **Ali Mohsin:** Writing – review & editing, Supervision, Resources, Project administration, Funding acquisition, Conceptualization.

Declaration of Generative AI and AI-assisted technologies in the writing process

This work utilized Grammarly's Generative AI just to improve the English language of the text. The author(s) fully reviewed and accurately edited the content as needed and take full responsibility for the published article's content.

Funding

This work was financially supported by the National Foreign Expert Program of China (Grant number: Y20240198), by the National Natural Science Foundation of China (Grant No. 22250410275), and also by Guangdong Basic and Applied Basic Research Foundation (Grant number: 2024A1515010433).

Declaration of competing interest

The authors declare that they have no known competing financial interests or personal relationships that could have appeared to influence the work reported in this paper.

Acknowledgements

This work was supported by the Shanghai Yeasen BioTechnologies Co., Ltd. The VDO Biotech (Suzhou) Co., Ltd. for assistance with Nanoflow Cytometer.

Appendix A. Supplementary data

Supplementary data to this article can be found online at https://doi.org/10.1016/j.cej.2026.174990.

Data availability

Data will be made available on request.

References

[1] D. Correa-Gallegos, D. Jiang, S. Christ, P. Ramesh, H.F. Ye, J. Wannemacher, S. K. Gopal, Q. Yu, M. Aichler, A. Walch, U. Mirastschijski, T. Volz, Y. Rinkevich, Patch repair of deep wounds by mobilized fascia, Nature 576 (Dec, 2019) 287–292, https://doi.org/10.1038/s41586-019-1794-y (Epub 2019 Nov 27. PMID: 31776510.).

[2] M.V. Plikus, C.F. Guerrero-Juarez, M. Ito, Y.R. Li, P.H. Dedhia, Y. Zheng, G. Cotsarelis, Regeneration of fat cells from myofibroblasts during wound healing, Science 355 (Feb 17, 2017) 748–752, https://doi.org/10.1126/science.aai8792 (Epub 2017 Jan 5. PMID: 28059714. PMCID: PMC5464786).

[3] Y.L. Song, Y.C. You, X.Y. Xu, J.Y. Liu, X.J. Huang, J.C. Zhang, L.W. Zhu, J.H. Hu, X. C. Wu, X.L. Xu, W.Q. Tan, Y.Z. Du, Adipose-derived mesenchymal stem cell-derived exosomes biopotentiated extracellular matrix hydrogels accelerate diabetic wound healing and skin regeneration, Adv. Sci. 10 (30) (Oct, 2023) 2304023, https://doi.org/10.1002/advs.202304023 (Epub 2023 Sep 15. PMID: 37712174. PMCID: PMC10602544).

[4] K.Y. Zhang, K. Cheng, Stem cell-derived exosome versus stem cell therapy, Nat. Rev. Bioeng. 1 (Apr, 2023) 608–609, https://doi.org/10.1038/s44222-023-00064-2 (PMID: 37359776. PMCID: PMC10092910).

[5] H. Wang, C.C. Huber, X.P. Li, Mesenchymal and neural stem cell-derived exosomes in treating Alzheimer's disease, Bioengineering 10 (Feb 15, 2023) 253–266, https://doi.org/10.3390/bioengineering10020253 (PMID: 36829747. PMCID: PMC9952071).

[6] E. Ali, N. Ghasem, S. Masoud, F. Hana, B. Saeid, H.K. Saeed, Application of exosomes for the regeneration of skin wounds: principles, recent applications and limitations, Tissue Cell 91 (Dec, 2024) 102611, https://doi.org/10.1016/j.tice.2024.102611 (Epub 2024 Nov 10. PMID: 39550901).

[7] L.M. Doyle, M.Z. Wang, Overview of extracellular vesicles, their origin, composition, purpose, and methods for exosome isolation and analysis, Cells 8 (Jul 15, 2019) 727–750, https://doi.org/10.3390/cells8070727 (PMID: 31311206. PMCID: PMC6678302).

[8] S. Gurunathan, M.H. Kang, M. Jeyaraj, M. Qasim, J.H. Kim, Review of the isolation, characterization, biological function, and multifarious therapeutic approaches of exosomes, Cells 8 (Apr 3, 2019) 307–342, https://doi.org/10.3390/cells8040307 (PMID: 30987213. PMCID: PMC6523673).

[9] X.X. Yang, C. Sun, L. Wang, X.L. Guo, New insight into isolation, identification techniques and medical applications of exosomes, J. Control. Release 308 (Aug 28, 2019) 119–129, https://doi.org/10.1016/j.jconrel.2019.07.021 (Epub 2019 Jul 17. PMID: 31325471).
[10] R. Maroto, Y. Zhao, M. Jamaluddin, V.L. Popov, H. Wang, M. Kalubowilage, Y. Zhang, J. Luisi, H. Sun, C.T. Culbertson, S.H. Bossmann, M. Motamedi, A. R. Brasier, Effects of storage temperature on airway exosome integrity for diagnostic and functional analyses, J. Extracell. Vesicles 6 (Aug 13, 2017) 1359478, https://doi.org/10.1080/20013078.2017.1359478 (eCollection 2017. PMID: 28819550. PMCID: PMC5556670).
[11] X. Zhang, Z. Chen, M. Jiang, Y. Lai, Y. Li, R. Yi, et al., Multifunctional swellable polymeric aerogel with thrombin and Maxpower for rapid hemostasis and antibacterial protection in gastrointestinal trauma, Adv. Healthc. Mater. 14 (32) (Dec, 2025) e02363, https://doi.org/10.1002/adhm.202502363 (Epub 2025 Aug 11. PMID: 40787763).
[12] X. Zhang, Y. Li, Y. Zhang, S. Wang, J. Zhao, T. Wang, Glutathione depletion-based pH-responsive injectable hydrogels for synergistic treatment of colon tumor, Int. J. Biol. Macromol. 297 (Mar, 2025) 139557, https://doi.org/10.1016/j.ijbiomac.2025.139557 (Epub 2025 Jan 6. PMID: 39778829).
[13] T. Harris, D. Trader, Exploration of degrons and their ability to mediate targeted protein degradation, RSC Med. Chem. (Jan 1, 2025) 39867589, https://doi.org/10.1039/d4md00787e (eCollection 2025 Mar 19. PMID: 39867589. PMCID: PMC11758578).
[14] C.Y. He, S.W. Bi, L. Zhang, J. Gu, B. Yan, An antioxidative sodium alginate hybrid hydrogel with NIR-controlled NO releasing for diabetic wound healing via reduced inflammation and enhanced angiogenesis, Carbohydr. Polym. 366 (Oct 15, 2025) 123913, https://doi.org/10.1016/j.carbpol.2025.123913 (Epub 2025 Jun 20. PMID: 40733834).
[15] T.S. Liu, H. Lei, L.L. Qu, C.H. Zhu, X.X. Ma, D.D. Fan, Algae-inspired chitosan-pullulan-based multifunctional hydrogel for enhanced wound healing, Carbohydr. Polym. 347 (Jan 1, 2025) 122751, https://doi.org/10.1016/j.carbpol.2024.122751 (Epub 2024 Sep 15. PMID: 39486980).
[16] Z.X. Yan, Q.L. Nie, J.J. Liu, J.X. Chen, Y.M. Liu, Y.D. Lu, M. Xu, Z.W. Lin, Sodium alginate/carboxymethyl chitosan/gelatin-naringenin pH-responsive hydrogel beads for oral delivery of traditional Chinese herbal medicines, Carbohydr. Polym. 366 (Oct 15, 2025) 123870, https://doi.org/10.1016/j.carbpol.2025.123870 (Epub 2025 Jun 11. PMID: 40733802).
[17] Y. Chen, X. Liu, R. Zhou, J.X. Qiao, J.T. Liu, R. Cai, J. Liu, J. Rong, L. Chen, Porous sodium alginate/cellulose nanofiber composite hydrogel microspheres for heavy metal removal in wastewater, Int. J. Biol. Macromol. 278 (3) (Oct, 2024) 135000, https://doi.org/10.1016/j.ijbiomac.2024.135000 (Epub 2024 Aug 22. PMID: 39181348).
[18] K. Zhang, H. Huang, Y. Zhao, Q. Zhen, D. Shi, J. Chen, X. Chen, Pullulan dialdehyde cross-linked dual-action adhesive with high adhesion to lung tissue and the capability of pH-responsive drug release, Carbohydr. Polym. 348 (Jan 15, 2025) 122906, https://doi.org/10.1016/j.carbpol.2024.122906 (Epub 2024 Oct 28. PMID: 39567140).
[19] T. Liu, H. Lei, L. Qu, C. Zhu, X. Ma, D.D. Fan, Algae-inspired chitosan–pullulan-based multifunctional hydrogel for enhanced wound healing, Carbohydr. Polym. 347 (Jan 1, 2025) 122751, https://doi.org/10.1016/j.carbpol.2024.122751 (Epub 2024 Sep 15. PMID: 39486980).
[20] A.Q. Chen, B.Y. Li, Q.F. Dang, C.Y. Liu, L.F. Shi, S.Y. Niu, D.S. Cha, Carboxymethyl chitosan/dialdehyde quaternized pullulan self-healing hydrogel loaded with tranexamic acid for rapid hemostasis, Carbohydr. Polym. 348 (Jan 15, 2025) 122817, https://doi.org/10.1016/j.carbpol.2024.122817 (Epub 2024 Oct. PMID: 39562092).
[21] Y. Cheng, X.X. Zhang, X.Y. Wu, Y.J. Ding, L.X. Zhu, J. Pan, M. Zhou, Multifunctional microneedle patches for perivascular gene delivery and treatment of vascular intimal hyperplasia, ACS Nano 18 (47) (Nov 26, 2024) 32578–32588, https://doi.org/10.1021/acsnano.4c09527 (Epub 2024 Nov 15. PMID: 39545708).
[22] L. Zong, R. Teng, H. Zhang, W. Liu, Y. Feng, Z. Lu, X. Pu, Ultrasound-responsive HBD peptide hydrogel with antibiofilm capability for fast diabetic wound healing, Adv. Sci. 11 (42) (Nov, 2024) e2406022, https://doi.org/10.1002/advs.202406022 (Epub 2024 Sep 9. PMID: 39248340. PMCID: PMC11558141).
[23] K.N. Niloofar, M. Elahe, A. Saeede, R.K. Mahmoud, R. Navid, K.O. Reza, Design and characterization of adipose-derived mesenchymal stem cell loaded alginate/pullulan/hyaluronic acid hydrogel scaffold for wound healing applications, Int. J. Biol. Macromol. 241 (Jun 30, 2023) 124556, https://doi.org/10.1016/j.ijbiomac.2023.124556 (Epub 2023 Apr 23. PMID: 40733834).
[24] J. Kim, M. Kang, G. Han, S. Hyung, M. Kim, M. Jang, et al., Meso–macroporous hydrogel for direct litre-scale isolation of extracellular vesicles, Nat. Nanotechnol. 20 (11) (Nov, 2025) 1678–1687, https://doi.org/10.1038/s41565-025-02011-1 (Epub 2025 Sep 24. PMID: 40993350; PMCID: PMC12623240).
[25] M. Barasinski, V. Jasper, M. Görke, G. Garnweitner, In situ tracking of nanoparticles during electrophoresis in hydrogels using a fiber-based UV-Vis system, Powders 4 (Jan 10, 2025), https://doi.org/10.3390/powders4010003.
[26] L. Yang, Z. Guo, W. Li, Q. Gou, L. Han, Q. Yu, The impact of lemon seeds oil microcapsules based on a bilayer macromolecule carrier on the storage of the beef jerky, Food Packag. Shelf Life 32 (Mar 16, 2022) 100838, https://doi.org/10.1016/j.fpsl.2022.100838.
[27] M.E. Mikhailova, A.V. Donets, V.B. Rogozhin, et al., Gellan and pullulan hydrogels of different molar mass, Nanotechnol. Russ. 20 (1) (Feb, 2025) 59–63, https://doi.org/10.1134/S2635167624602523.
[28] Y. Yi, J. Song, P. Zhou, Y. Shu, P. Liang, H. Liang, et al., An ultrasound-triggered injectable sodium alginate scaffold loaded with electrospun microspheres for on-demand drug delivery to accelerate bone defect regeneration, Carbohydr. Polym. 334 (Jun, 2024) 122039, https://doi.org/10.1016/j.carbpol.2024.122039 (Epub 2024 Mar 11. PMID: 38553236).
[29] H. Weng, W. Zou, F. Tian, H. Xie, A. Liu, W. Liu, et al., Inhalable cardiac targeting peptide modified nanomedicine prevents pressure overload heart failure in male mice, Nat. Commun. 15 (1) (Jul, 2024) 6058, https://doi.org/10.1038/s41467-024-50312-1 (PMID: 39025877; PMCID: PMC11258261).
[30] L.A. Haines, A.A. Baeckler, S.J. Schofield, E.P. Palmer, B.F. Guilliams, M.A. Meyers, D.P. Regan, Non-specific particle formation during extracellular vesicle labelling with the lipophilic membrane dye PKH26, J. Extracell. Vesicles 14 (5) (May, 2025) e70079, https://doi.org/10.1002/jev2.70079 (PMID: 40387660; PMCID: PMC12087298).
[31] B. Yang, Z. Li, Z. Yang, P. Zhao, S. Lin, J. Wu, et al., Recapitulating hypoxic metabolism in cartilaginous organoids via adaptive cell-matrix interactions enhances histone lactylation and cartilage regeneration, Nat. Commun. 16 (1) (Mar, 2025) 2711, https://doi.org/10.1038/s41467-025-57779-6 (PMID: 40108220; PMCID: PMC11923171).
[32] C.Y. Zhong, Y. Zhang, Y. Liu, K. Zeng, L. Fan, Q. Wang, J. Zhang, Adhesive hydrogel based on Konjac Glucomannan (KGM) loaded with siACTC1-exosomes for enhanced post-surgical keloid treatment, Int. J. Biol. Macromol. 319 (Part 3) (Aug, 2025) 145360, https://doi.org/10.1016/j.ijbiomac.2025.145360 (Epub 2025 Jun 20. PMID: 40545090).
[33] M.J. Borrelli, B. Kolendowski, G.E. DiMattia, T.G. Shepherd, Spatiotemporal analysis of ratiometric biosensors in live multicellular spheroids using SPoRTS, Cell Rep. Methods 5 (2) (Feb, 2025) 100987, https://doi.org/10.1016/j.crmeth.2025.100987 (Epub 2025 Feb 17. PMID: 39965566; PMCID: PMC11955269).
[34] M. O'Mara, S. Zhang, U.G. Knaus, Spatiotemporal H2O2 flashes coordinate actin cytoskeletal remodeling and regulate cell migration and wound healing, Nat. Commun. 16 (1) (Jul, 2025) 6868, https://doi.org/10.1038/s41467-025-62272-1 (PMID: 40715145; PMCID: PMC12297405).
[35] Y. Cao, H.L. Cong, B. Yu, Y.Q. Shen, A review on the synthesis and development of alginate hydrogels for wound therapy, J. Mater. Chem. B 11 (Mar 30, 2023) 2801–2829, https://doi.org/10.1039/d2tb02808e (PMID: 36916313).
[36] A. Richardson, S. Fok, V. Lee, K.A. Rye, N. Di Girolamo, B.J. Cochran, Use of high-refractive index hydrogels and tissue clearing for large biological sample imaging, Gels 8 (1) (Jan 4, 2022) 32, https://doi.org/10.3390/gels8010032 (PMID: 35049567. PMCID: PMC8774797).
[37] T. Li, X.B. Song, C.M. Weng, X. Wang, L. Sun, X.Y. Gong, C. Chen, Self-crosslinking and injectable chondroitin sulfate/pullulan hydrogel for cartilage tissue engineering, Appl. Mater. Today 10 (Dec 15, 2017) 173–183, https://doi.org/10.1016/j.apmt.2017.12.002.
[38] M. Sirajuddin, S. Ali, A. Badshah, Drug-DNA interactions and their study by UV-visible, fluorescence spectroscopies and cyclic voltammetry, J. Photochem. Photobiol. B 124 (Jul 5, 2013) 1–19, https://doi.org/10.1016/j.jphotobiol.2013.03.013 (Epub 2013 Apr 6. PMID: 23648795).
[39] M.M. Conradie, Cu(β-diketonato)$_2$ bathochromic shifts from the ultraviolet towards the visible region, J. Mol. Model. 30 (10) (Sep 17, 2024) 336, https://doi.org/10.1007/s00894-024-06138-1 (PMID: 39287699. PMCID: PMC11408553).
[40] N.J. Hestand, F.C. Spano, Molecular aggregate photophysics beyond the Kasha model: novel design principles for organic materials, Acc. Chem. Res. 50 (2) (Feb 21, 2017) 341–350, https://doi.org/10.1021/acs.accounts.6b00576 (Epub 2017 Feb 1. PMID: 28145688).
[41] Z. Belattmania, S. Kaidi, S. El Atouani, C. Katif, F. Bentiss, C. Jama, V. Vasconcelos, Isolation and FTIR-ATR and ^{1}H NMR characterization of alginates from the main alginophyte species of the Atlantic Coast of Morocco, Molecules 25 (18) (Sep 22, 2020) 4335, https://doi.org/10.3390/molecules25184335 (PMID: 32971782. PMCID: PMC7570942).
[42] J. Li, Z.S. Wang, W.J. Yang, Y.C. Zhou, F. Tao, Y.H. Zhang, Y. Xie, Hypoxia-preconditioned ADSC exosomes encapsulated in a multifunctional dual-network hydrogel promote healing and functional regeneration of seawater-immersed wounds, Chem. Eng. J. 518 (Aug 15, 2025) 164717, https://doi.org/10.1016/j.cej.2025.164717.
[43] Y. Fang, J.H. Shi, J. Liang, D. Ma, H.M. Wang, Water-regulated viscosity–plasticity phase transitions in a peptide self-assembled muscle-like hydrogel, Nat. Commun. 16 (1) (Jan 26, 2025) 1058, https://doi.org/10.1038/s41467-025-56415-7 (PMID: 39865087. PMCID: PMC11770121).
[44] T.I. Gromovykh, I.A. Tarasova, V.V. Zefirov, A.A. Gulin, I.P. Ivanenko, V. S. Molchanov, O.I. Kiselyova, Composites of bacterial cellulose and alginate produced in situ: the impact of viscosity and temperature on microscale morphology, Carbohydr. Polym. 357 (Jun 1, 2025) 123495, https://doi.org/10.1016/j.carbpol.2025.123495 (Epub 2025 Mar 10. PMID: 40159012).
[45] Y. Zhang, J. Bi, J. Huang, Y. Tang, S. Du, P. Li, Exosome: a review of its classification, isolation techniques, storage, diagnostic and targeted therapy applications, Int. J. Nanomedicine 15 (Sep 22, 2020) 6917–6934, https://doi.org/10.2147/IJN.S264498 (eCollection 2020. PMID: 33061359. PMCID: PMC7519827).
[46] M.B. Łabowska, M. Skrodzka, H. Sicińska, I. Michalak, J. Detyna, Influence of cross-linking conditions on drying kinetics of alginate hydrogel, Gels 9 (1) (Jan 1, 2023) 63, https://doi.org/10.3390/gels9010063 (PMID: 36661829. PMCID: PMC9858758).
[47] Y. Zhang, W. Yan, L. Wu, Z. Yu, Y. Quan, X. Xie, Different exosomes are loaded in hydrogels for the application in the field of tissue repair, Front. Bioeng. Biotechnol. 13 (Mar 3, 2025) 1545636, https://doi.org/10.3389/fbioe.2025.1545636 (eCollection 2025. PMID: 40099037. PMCID: PMC11911322).
[48] Z. Németh, I. Csóka, R. Semnani Jazani, B. Sipos, H. Haspel, G. Kozma, D.G. Dobó, Quality-by-design-driven zeta potential optimization of liposomes with charge-

imparting membrane additives, Pharmaceutics 14 (9) (Aug 26, 2022) 1798, https://doi.org/10.3390/pharmaceutics14091798 (PMID: 36145546. PMCID: PMC9503861).
[49] X.Q. Diao, Y. Wang, R.X. Jia, X.D. Chen, G.H. Liu, D.Y. Liu, Influences of ultrasonic treatment on the physicochemical properties and microstructure of diacylglycerol-loaded emulsion stabilized with soybean protein isolate and sodium alginate, Ultrason. Sonochem. 108 (Aug, 2024) 1350–1417, https://doi.org/10.1016/j.ultsonch.2024.106981 (Epub 2024 Jul 6. PMID: 38981339. PMCID: PMC11280087).
[50] N.A. Coman, M. Babotă, A. Nicolescu, A. Nicolae-Maranciuc, L. Berta, A. Man, C. Tanase, Biosynthesis of palladium nanoparticles using aqueous bark extract of Quercus species for antioxidant and antimicrobial applications, Plants 13 (23) (Dec 3, 2024) 3390, https://doi.org/10.3390/plants13233390 (PMID: 39683182. PMCID: PMC11644216).
[51] D. Andreucci, E. Cirillo, M. Colangeli, D. Gabrielli, Fick and Fokker–Planck diffusion law in inhomogeneous media, J. Stat. Phys. 174 (2) (Oct 30, 2019) 469–493, https://doi.org/10.1007/s10955-018-2187-6.
[52] X. Xu, Y. Pang, X. Fan, Mitochondria in oxidative stress, inflammation and aging: mechanisms and therapeutic advances, Signal Transduct. Target. Ther. 10 (1) (Jun 11, 2025) 190, https://doi.org/10.1038/s41392-025-02253-4 (PMID: 40500258. PMCID: PMC12159213).
[53] W.Y. Guo, Q.M. Wu, H.F. Zeng, Y.L. Chen, J. Xu, Z.Y. Yu, H.D. Pan, A sinomenine derivative alleviates bone destruction in arthritis by suppressing mitochondrial dysfunction via NRF2/HO-1/NQO1 pathway, Pharmacol. Res. 215 (May, 2025) 107686, https://doi.org/10.1016/j.phrs.2025.107686 (Epub 2025 Mar 13. PMID: 40088961).
[54] S.R. Stevenson, S.B. Tzokov, I. Lahiri, K.R. Ayscough, P.A. Bullough, Cryo-EM reconstruction of yeast ADP-actin filament at 2.5 Å, Structure 33 (3) (Mar 6, 2025) 435–442.e3, https://doi.org/10.1016/j.str.2024.12.008 (Epub 2025 Jan 10. PMID: 39798573).
[55] E.T. Schmid, J.M. Schinaman, N. Liu-Abramowicz, K.S. Williams, D.W. Walker, Accumulation of F-actin drives brain aging and limits healthspan in Drosophila, Nat. Commun. 15 (1) (Oct 25, 2024) 9238, https://doi.org/10.1038/s41467-024-53389-w (PMID: 39455560. PMCID: PMC11512044).
[56] W. Kong, Y. Bao, W. Li, D. Guan, Y. Yin, Y. Xiao, Z. Xia, Collaborative enhancement of diabetic wound healing and skin regeneration by recombinant human collagen hydrogel and hADSCs, Adv. Healthc. Mater. 13 (29) (Nov, 2024) e2401012, https://doi.org/10.1002/adhm.202401012 (Epub 2024 Oct 10. PMID: 39388509).
[57] E. Jin, Y. Yang, S. Cong, D. Chen, R. Chen, J. Zhang, W. Chen, Lemon-derived nanoparticle-functionalized hydrogels regulate macrophage reprogramming to promote diabetic wound healing, J. Nanobiotechnol. 23 (1) (Jan 31, 2025) 68, https://doi.org/10.1186/s12951-025-03138-y (PMID: 39891270. PMCID: PMC11783766).
[58] D. Zhu, Z. Chen, K. Guo, Q. Xie, Y. Zou, Q. Mou, G. Jin, Enhanced viability and functional maturity of iPSC-derived islet organoids by collagen VI–enriched ECM scaffolds, Cell Stem Cell 32 (4) (Apr 3, 2025) 547–563, https://doi.org/10.1016/j.stem.2025.02.001 (e7. Epub 2025 Feb 24. PMID: 39999846).
[59] Y. Xu, Q. Bian, Y. Zhang, Y. Zhang, D. Li, X. Ma, J. Gao, Single-dose bilayer microneedles for enhanced hypertrophic scar therapy with rapid anti-inflammatory and sustained inhibition of myofibroblasts, Biomaterials 312 (Jan, 2025) 122742, https://doi.org/10.1016/j.biomaterials.2024.122742 (Epub 2024 Jul 31. PMID: 39106821).
[60] Y.H. Xu, C. Wei, L. Ma, Z. Long, D.F. Li, Y.L. Lin, F.Y. Wang, 3D mesenchymal stem cell exosome-functionalized hydrogels for corneal wound healing, J. Control. Release 380 (Apr, 2025) 630–646, https://doi.org/10.1016/j.jconrel.2025.02.030 (Epub 2025 Feb 16. PMID: 39955036).
[61] Y.S. Yuan, H.Y. Li, H. Lu, G.C. Li, Z. Cao, C. Xu, H.L. Xu, Reprogramming mitochondrial metabolism to enhance macrophage polarization by ROS-responsive nanoparticles for osteoarthritis, Biomaterials 322 (Nov, 2025) 123395, https://doi.org/10.1016/j.biomaterials.2025.123395 (Epub 2025 May 7. PMID: 40403559).
[62] X. Cheng, H. Sui, F. Chen, C. Li, M. Du, S. Zhang, H. Huang, Nanomaterial-mediated reprogramming of macrophages to inhibit refractory muscle fibrosis, Adv. Mater. 36 (52) (Dec, 2024) e2410368, https://doi.org/10.1002/adma.202410368 (Epub 2024 Nov 16. PMID: 39548911. PMCID: PMC11849413).
[63] R. Yang, J. Wang, X. Chen, Y. Shi, J. Xie, Epidermal stem cells in wound healing and regeneration, Stem Cells Int. (Jan 29, 2020) 914831, https://doi.org/10.1155/2020/9148310 (eCollection 2020. PMID: 32399054. PMCID: PMC7204129).
[64] H.E. Talbott, S. Mascharak, M. Griffin, D.C. Wan, M.T. Longaker, Wound healing, fibroblast heterogeneity and fibrosis, Cell Stem Cell 29 (8) (Aug 4, 2022) 1161–1180, https://doi.org/10.1016/j.stem.2022.07.006 (PMID: 35931028. PMCID: PMC9357250).
[65] O. Blaise, C. Duchesne, E. Capuzzo, M.A. Nahori, J. Fernandes, M.G. Connor, Infected wound repair correlates with collagen I induction and NOX2 activation by cold atmospheric plasma, npj Regener. Med. 9 (1) (Oct 2, 2024) 28, https://doi.org/10.1038/s41536-024-00372-0 (PMID: 39358383. PMCID: PMC11447178).
[66] S.A. Eming, P. Martin, M.T. Canic, Wound repair and regeneration: mechanisms, signaling and translation, Sci. Transl. Med. 6 (Dec 3, 2014) 265sr6, https://doi.org/10.1126/scitranslmed.3009337 (PMID: 25473038. PMCID: PMC4973620).
[67] F.S. Younesi, A.E. Miller, T.H. Barker, Fibroblast and myofibroblast activation in normal tissue repair and fibrosis, Nat. Rev. Mol. Cell Biol. 25 (Aug, 2024) 617–638, https://doi.org/10.1038/s41580-024-00716-0 (Epub 2024 Apr 8. PMID: 38589640).
[68] I. Ballesteros, A. Hidalgol, The neutrophil collective, Cell 188 (25) (Dec 11, 2025) P7019–P7035, https://doi.org/10.1016/j.cell.2025.11.001 (PMID: 41386219).
[69] M.L. Ford, M.I. Reza, A. Ruwanpathirana, V. Sathish, R.D. Britt Jr., Integrative roles of pro-inflammatory cytokines on airway smooth muscle structure and function in asthma, Immunol. Rev. 330 (1) (Mar, 2025) e70007, https://doi.org/10.1111/imr.70007 (PMID: 39991781. PMCID: PMC11848829).
[70] M. Hunt, M. Torres, E. Bachar-Wikstrom, J. Wikatrom, Cellular and molecular roles of reactive oxygen species in wound healing, Commun. Biol. 7 (Nov 19, 2024) 1534, https://doi.org/10.1038/s42003-024-07219-w (PMID: 39562800. PMCID: PMC11577046).
[71] M. Nayak, D. Banerjee, V. Venugopal, S.K. Nethi, A.K. Barui, S. Mukherjee, Cell-engineered technologies for wound healing and tissue regeneration, npj Biomed. Innov. 2 (Oct 24, 2025) 38, https://doi.org/10.1038/s44385-025-00042-w.
[72] D. Pranantyo, C.K. Yeo, Y. Wu, C. Fan, X.F. Xu, Y.S. Yip, M.I.G. Vos, Hydrogel dressings with intrinsic antibiofilm and antioxidative dual functionalities accelerate infected diabetic wound healing, Nat. Commun. 15 (Feb 1, 2024) 954, https://doi.org/10.1038/s41467-024-44968-y (PMID: 38296937. PMCID: PMC10830466).